CMIP6 Model-Projected Hydroclimatic and Drought Changes and Their Causes in the Twenty-First Century

TIANBAO ZHAO[a] AND AIGUO DAI[b]

[a] *Key Laboratory of Regional Climate-Environment Research for Temperate East Asia, Institute of Atmospheric Physics, Chinese Academy of Sciences, Beijing, China*

[b] *Department of Atmospheric and Environmental Sciences, University at Albany, State University of New York, Albany, New York*

(Manuscript received 10 June 2021, in final form 1 November 2021)

ABSTRACT: Drought is projected to become more severe and widespread as global warming continues in the twenty-first century, but hydroclimatic changes and their drivers are not well examined in the latest projections from phase 6 of the Coupled Model Intercomparison Project (CMIP6). Here, precipitation (P), evapotranspiration (E), soil moisture (SM), and runoff (R) from 25 CMIP6 models, together with self-calibrated Palmer drought severity index with Penman–Monteith potential evapotranspiration (scPDSIpm), are analyzed to quantify hydroclimatic and drought changes in the twenty-first century and the underlying causes. Results confirm consistent drying in these hydroclimatic metrics across most of the Americas (including the Amazon), Europe and the Mediterranean region, southern Africa, and Australia, although the drying magnitude differs, with the drying being more severe and widespread in surface SM than in total SM. Global drought frequency based on surface SM and scPDSIpm increases by ~25%–100% (50%–200%) under the SSP2-4.5 (SSP5-8.5) scenario in the twenty-first century together with large increases in drought duration and areas, which result from a decrease in the mean and flattening of the probability distribution functions of SM and scPDSIpm, while the R-based drought changes are relatively small. Changes in both P and E contribute to the SM change, whereas scPDSIpm decreases result from ubiquitous PET increases and P decreases over subtropical areas. The R changes are determined primarily by P changes, while the PET change explains most of the E increase. Intermodel spreads in surface SM and R changes are large, leading to large uncertainties in the drought projections.

SIGNIFICANCE STATEMENT: Drought may become more severe and widespread under greenhouse gas (GHG)-induced global warming in the twenty-first century based on model projections. However, there are still large uncertainties in projected future drought changes, especially regarding the extent to which drought changes depend on drought indices and the future emissions scenarios analyzed. The latest projections from CMIP6 models reaffirm the widespread drying and increases in agricultural drought by up to 200% over most of the Americas (including the Amazon), Europe and the Mediterranean region, southern Africa, Southeast Asia, and Australia under moderate-to-high emissions scenarios in the twenty-first century, despite large uncertainties in individual projections partly due to internal variability. Ubiquitous increases in atmospheric demand for moisture under rising temperatures and precipitation decreases over many subtropical regions are the main driver of the projected drying and drought increases.

KEYWORDS: Drought; Climate change; Hydrology; Climate models

1. Introduction

Drought is among the most damaging natural hazards, often causing severe losses to agriculture, ecosystems, and human societies (Easterling et al. 2000; Dai 2011a; Giorgi et al. 2018). Drought can persist for a period of weeks or longer with reduced precipitation and is often intensified through a positive feedback loop, in which dry soils and diminished vegetation cover can further suppress precipitation through reduced evapotranspiration and enhanced surface warming (Dai et al. 2018). Historical records of precipitation, streamflow, and observation-derived drought indices all show increased aridity since 1950 over Africa, southern Europe, East Asia, eastern Australia, northwest Canada, and southern Brazil (e.g., Dai 2011a,b, 2013a, 2021; Dai and Zhao 2017), although some of the regional drying trends may be related to internal multidecadal climate variability (Dai 2021). Model-simulated soil moisture, runoff, drought indices, and precipitation minus evaporation ($P - E$) suggest increased risk of drought over most land areas in the twenty-first century under greenhouse gas (GHG)-induced global warming (e.g., Wang 2005; Burke et al. 2006; Burke and Brown 2008; Sheffield and Wood 2008; Dai 2011a, 2013a; Wehner et al. 2011; Taylor et al. 2013; Fu and Feng 2014; Prudhomme et al. 2014; Cook et al. 2014, 2015, 2018, 2020; Dai et al. 2018; Zhao and Dai 2015, 2017; Berg and Hall 2017; Berg et al. 2017; Zhang et al. 2019), due to decreased precipitation over many subtropical land areas

Supplemental information related to this paper is available at the Journals Online website: https://doi.org/10.1175/JCLI-D-21-0442.s1.

Corresponding authors: Aiguo Dai, adai@albany.edu; Tianbao Zhao, zhaotb@tea.ac.cn

DOI: 10.1175/JCLI-D-21-0442.1

© 2022 American Meteorological Society. For information regarding reuse of this content and general copyright information, consult the AMS Copyright Policy (www.ametsoc.org/PUBSReuseLicenses).

Brought to you by SUNY ALBANY LIBR SB23 | Unauthenticated | Downloaded 01/06/22 06:58 PM UTC

and increased atmospheric demand for moisture due to increased water vapor pressure deficit under rising air temperatures (Scheff and Frierson 2014; Zhao and Dai 2015; Dai et al. 2018). However, there are large uncertainties in the projected drought and other hydroclimatic changes over the twenty-first century, partly because of large internal variability (Dai et al. 2018) and a wide range of responses to rising GHGs among global climate models associated with different model physics and varying emissions scenarios (Knutti and Sedlacek 2013; Cook et al. 2014, 2018, 2020; Berg et al. 2017; Dai et al. 2018; Vicente-Serrano et al. 2020). In particular, the key drivers of the projected hydroclimatic and drought changes are not well understood, as most studies focused mainly on quantifying the changes, rather than the underlying physical processes.

Many studies show that large increases in evaporative demand for moisture or potential evapotranspiration (PET) are a major driver for increased aridity (Feng and Fu 2013; Fu and Feng 2014; Scheff and Frierson 2014, 2015; Cook et al. 2014; Zhao and Dai 2015), whereas drought indices based on precipitation alone (such as the standardized precipitation index, SPI) or $P - E$ cannot account for the increasing evaporative demand in a warming climate. Thus, it is necessary to use those drought indices that include the effect of PET, such as normalized soil moisture content, runoff, and the improved Palmer drought severity index (PDSI; Palmer 1965; Dai 2011b), to quantify drought changes under global warming (Dai 2011a). The ubiquitous PET increase over global land results mainly from increased vapor pressure deficit under rising surface air temperatures (Scheff and Frierson 2014, 2015; Zhao and Dai 2015) and small decreases in surface relative humidity over land (Chen et al. 2020). Over many subtropical areas, such as southern Europe and southwest North America, reduced precipitation further increases the risk of drought greatly, and the subtropical precipitation decrease is attributed to increased drying by subsidence due to increased vertical gradients of specific humidity (Chou et al. 2009), expansion of the subtropical drying zone (Lu et al. 2007; Scheff and Frierson 2012), and increased downward motion (Dai et al. 2018).

Zhao and Dai (2015) examined the magnitude and causes of drought changes over global land under a low-to-moderate emissions scenario (RCP4.5) from 14 models participated in phase 5 of the Coupled Model Intercomparison Project (CMIP5). In contrast to some earlier studies, they found that the relationship between the self-calibrated PDSI (Wells et al. 2004) with the Penman–Monteith PET (scPDSIpm) and topsoil moisture content or runoff is similar during the current and future climates, and the drought frequency change patterns based on these different drought indices are comparable in the twenty-first century. However, the magnitude of the drought change varies substantially among the three drought indices. Zhao and Dai (2015) also found that the probability distribution functions (PDFs) of the topsoil moisture, scPDSIpm, and runoff become wider in the twenty-first century over most land areas (which include changes in the mean seasonal cycle), contributing to increased drought events. Zhao and Dai (2017) further compared the CMIP3 and CMIP5 model-projected drought changes and found similar long-term changes in global and hemispheric drought frequency and drought areas estimated based on scPDSIpm. Berg et al. (2017) analyzed soil moisture changes at different depths from 25 CMIP5 models and found that the drying is most pronounced in the topsoil layer, even in some regions of the northern mid- to high latitudes where total soil water may increase presumably due to large precipitation increases there. Zhang et al. (2019) investigated the reservoirs (e.g., precipitable water and soil moisture) and water fluxes (e.g., precipitation P, evaporation E, $P - E$, and total runoff R) of the water cycle under the RCP8.5 scenario from 27 CMIP5 models; they found that the water cycle over the global monsoon regions will intensify with global warming, and the increased seasonality and drier soils throughout the year imply reductions in crop yields and increased flood and drought risks.

Recently, Cook et al. (2020) further investigated drought and mean hydroclimatic changes (in P, R, and soil moisture SM) in the twenty-first century under three Shared Socioeconomic Pathways (namely, SSP1-2.6, SSP2-4.5, and SSP3-7.0; Meinshausen et al. 2020) using simulations from 13 CMIP6 models (Eyring et al. 2016). They found that the drying and drought frequency increases based on soil moisture and runoff changes are more robust, spatially more extensive, and more severe than those based on precipitation change. However, they did not examine scPDSIpm-based drought changes using the CMIP6 simulations, nor did they investigate the major drivers of the drought and hydroclimatic changes in the CMIP6 models. In particular, it is unclear whether the flattening of the histograms, with increased standard deviations (SDs) and reduced peak frequencies in addition to a shift in the mean, of the scPDSIpm, topsoil moisture, and runoff found in CMIP5 models (Zhao and Dai 2015) is evident in the new CMIP6 projections.

In this study, we further assess the magnitudes, spatial patterns, and causes of the mean changes in hydroclimatic fields and in agricultural and hydrological droughts in the twenty-first century based on the scPDSIpm, surface and total soil moisture content, and surface and total runoff from simulations by 25 CMIP6 models under a low-to-moderate scenario (SSP2-4.5) and a high emissions scenario (SSP5-8.5) available at the time we started the analysis. Following Zhao and Dai (2015), we focus on the changes in the histograms of the hydroclimatic variables and the key drivers of the changes. Different from Zhao and Dai (2015), we compare the changes under the two different scenarios, in surface and total soil moisture, and in surface and total runoff, examine drought duration changes (not analyzed in Zhao and Dai 2015), and present a more comprehensive analyses of the mean changes in these hydroclimatic fields. The comparison between surface and total soil moisture changes is of interest because Berg et al. (2017) found reduced drying in subsurface layers in CMIP5 models, which suggests that surface drying caused by increased PET may take a long time to penetrate into deeper layers.

The paper is organized as follows: section 2 describes the model data and analysis method. Hydroclimatic and drought changes in the twenty-first century over global land and in several hotspot regions are discussed in section 3. In section 4,

Brought to you by SUNY ALBANY LIBR SB23 | Unauthenticated | Downloaded 01/06/22 06:58 PM UTC

TABLE 1. A list of the CMIP6 models used in this study. Only one run (r1ip1f1) was used for each model. Data from the large ensemble of the 50-member runs (including soil moisture and runoff) from CanESM5 were also analyzed.

Model name	Modeling center	Lon× lat dimensions	References[a]
ACCESS-CM2	CSIRO-ARCCSS	144 × 72	Dix et al. (2019a,b)
ACCESS-ESM1-5	CSIRO	144 × 72	Ziehn et al. (2019a,b, 2020)
AWI-CM-1-1-MR[b,c,d,e]	AWI	144 × 72	Semmler et al. (2018, 2019)
BCC-CSM2-MR	BCC	320 × 160	Wu et al. (2018), Xin et al. (2019)
CanESM5	CCCma	128 × 64	Swart et al. (2019a,b,c)
CESM2	NCAR	288 × 192	Danabasoglu (2019a,b)
CESM2-WACCM	NCAR	144 × 72	Danabasoglu (2019c,d)
CMCC-CM2-SR5	CMCC	288 × 192	Lovato and Peano (2020a,b)
EC-Earth3	EC-EARTH consortium	256 × 128	EC-Earth Consortium (2019a,b)
EC-Earth3-Veg	EC-EARTH consortium	192 × 96	EC-Earth Consortium (2019c,d)
FGOALS-f3-L	CAS	128 × 60	Yu (2019a,b)
FGOALS-g3	CAS	192 × 145	Li (2019a,b)
GFDL-CM4	GFDL	288 × 180	Guo et al. (2018a,b)
GFDL-ESM4[d]	GFDL	288 × 180	John et al. (2018), Krasting et al. (2018)
INM-CM4-8[b]	INM	192 × 145	Volodin et al. (2019a,b)
INM-CM5-0[b]	IIM	192 × 145	Volodin et al. (2019c,d)
IPSL-CM6A-LR	IPSL	96 × 95	Boucher et al. (2018, 2019)
KACE-1-0-G[c]	NIMS-KMA	192 × 144	Byun et al. (2019a,b)
MIROC6	MIROC	256 × 128	Tatebe and Watanabe (2018), Shiogama et al. (2019)
MPI-ESM1-2-HR	MPI-M	256 × 128	Jungclaus et al. (2019), Wieners et al. (2017)
MPI-ESM1-2-LR	MPI-M	256 × 128	Wieners et al. (2019a,b)
MRI-ESM2-0	MRI	320 × 160	Yukimoto et al. (2019a,b)
NorESM2-LM	NCC	144 × 96	Seland et al. (2019a,b)
NorESM2-MM	NCC	320 × 160	Bentsen et al. (2019a,b)
UKESM1-0-LL	MOHC	192 × 144	Good et al. (2019), Tang et al. (2019)

[a] These references are listed in the supplemental material.
[b] Top-10-cm soil moisture data were unavailable.
[c] Total moisture data were unavailable.
[d] Surface runoff data were unavailable.
[e] Total runoff data were unavailable.

the magnitude and causes of the future hydroclimate and drought changes are examined. A summary and conclusions are presented in section 5.

2. Data and method

a. Model data and drought definition

We analyzed monthly data from all-forcing historical simulations from 1850 to 2014 and the twenty-first century projections from 2015 to 2100 from 25 CMIP6 models (one run per model) available at the time we started the analysis (Table 1) under two emissions scenarios: the SSP2-4.5 (global radiative forcing of 4.5 W m^{-2} by 2100, middle-of-the-road pathway, slightly higher than ~4.0 W m^{-2} for RCP4.5) and SSP5-8.5 (8.5 W m^{-2} forcing, high-end forcing pathway). The variables used in this study include precipitation (P), surface air temperature (T), net radiation (including net surface longwave radiation LW and shortwave radiation SW), specific humidity (q), wind speed (WS), air pressure, top-10-cm-layer soil moisture content (SM), total SM, surface runoff (R), total R, and evapotranspiration (E). However, some of these variables may not be provided by some models for all the simulations. For example, the top-10-cm SM and the total SM were available only from 22 and 23 models, while surface R and total R were available from 23 and 24 of the models, respectively. We used all the available models in the multimodel ensemble mean to increase its representativeness and minimize the internal noise. The incomparability resulting from the small change in the number of models should be small.

Following Zhao and Dai (2015), all model data were first regridded onto a 2.5° latitude × 2.5° longitude grid using a scheme that conserves the quantity locally and globally before further analysis. The monthly scPDSIpm (Dai 2011b) along with the PET based on the Penman–Monteith equation (Shuttleworth 1993) were computed for each of the 25 model runs using the regridded model data. The regridded model data and the offline-calculated scPDSIpm and PET were simply averaged over all the models (one run per model) to derive the multimodel ensemble mean (MMM). For the scPDSIpm calculation, the 1950–79 was used as the calibration period in order to avoid including the large anthropogenic climate change since 1980 as part of the natural variability used in the calibration (Dai 2011b, 2013a; Dai and Zhao 2017). For all the variables, the 1970–99 mean was used as the reference baseline and subtracted from the monthly data at each grid box before regional averaging and other analysis.

Before analyzing changes in drought frequency, duration, and area, which represent changes in dry extremes, we also examined the mean changes in several hydroclimatic fields,

Brought to you by SUNY ALBANY LIBR SB23 | Unauthenticated | Downloaded 01/06/22 06:58 PM UTC

including P, E, SM, R, and scPDSIpm, as well as the changes in their PDFs. A decease in the mean of P, SM, R, and scPDSIpm would suggest a drying trend toward more arid conditions, and imply increased risks of drought. However, although the mean and extreme (e.g., drought) changes are related, the two are not the same, as noticed previously (Dai et al. 2018). Here, we use "drying" to refer to a mean change toward a drier condition, and "increases in drought" to refer to increases in the occurrence of drought events, which are represented by the left tail of the PDFs of the drought indices.

To improve the spatial comparability of drought frequency, we defined a drought event as a period of consecutive months with local monthly drought index below the value corresponding to the 20th percentile of the current (1970–99) climate, which corresponds to the moderate drought examined in Zhao and Dai (2015). The SM and R anomalies were normalized by local SD of the 1970–99 period (separately for each month) for each model before being used to define agricultural and hydrological drought based on the 20th percentile, respectively. In addition, we calculated the mean drought duration (in months) locally as the consecutive months under drought conditions averaged over all drought events. The drought frequency and mean duration based on the scPDSIpm, normalized SM and R indices were first derived for each model run and then averaged over the models to derive their MMM changes.

Besides examining global maps and time series of global averages, histogram changes are also investigated for four hotspot regions outlined in Fig. 1a of Zhao and Dai (2015). They are the western United States (31.25°–48.75°N, 121.25°–103.75°W), southern Europe (38.75°–51.25°N, 11.25°W–28.75°E), southern Africa (33.75°–16.25°S, 13.75°–33.75°E), and the Amazon (11.25°S–1.25°N, 76.25°–48.75°W). PDFs were derived for each model by spline-fitting the histograms of the occurrence frequency estimated using local monthly anomalies (relative to 1970–99 monthly climatology but with the annual-mean change being removed) from all grid cells within each of the four hotspot regions for the present (1970–99) or future (2070–99) periods. The monthly anomalies of the soil moisture and runoff were normalized at each grid box by the SD of the 1970–99 period (separately for each month) before estimating the histograms. The PDFs for individual models (without annual-mean change) were then averaged over the models to derive the multimodel ensemble mean PDFs. The removal of the annual-mean change ensures that different climate responses to the same forcing among different models would not increase the spread of the multimodel averaged PDFs, while the inclusion of the future change in the mean annual cycle in the PDF calculation makes it consistent with the calculation of future drought changes that are based on the anomalies relative the current monthly climatology. As in Donat and Alexander (2012), the significance in the PDF changes between the two time periods were tested using a Student's t test (to test if the sample means are different) and F test (to test whether the sample variances are drawn from different populations). Besides the single run from 25 CMIP6 models, the 50-member ensemble runs from CanESM5 under SSP-4.5 and SSP5-8.5 were also analyzed to investigate the PDF changes in soil moisture and runoff over the four hotspot regions.

b. Attribution analysis

In this paper, we perform analyses similar to those done by Zhao and Dai (2015) to attribute the scPDSIpm changes to individual drivers in the twenty-first century under two emissions scenarios. Here, we briefly summarized this attribution analysis. The scPDSIpm from 25 model runs were first computed separately for each case in which only one forcing factor was allowed to change (from 1900 to 2100) while all others were kept at the values of the 1950–79 monthly climatology for years outside 1950–79 (i.e., during the 1950–79 calibration period, all variations were allowed and thus it is the same for all cases). Thus, the scPDSIpm was computed for one all-forcing case (i.e., all variables allowed to change), and five individual forcing cases (for changes in P, $T + q$, LW, SW and WS alone), leading to a total of 150 different PDSI datasets (6 for each model) for each scenario. Each of these cases was then ensemble-averaged over the 25 models, and the ensemble mean differences between the current (1970–99) and future (2070–99) periods were used to estimate the mean contributions from the individual forcing factors. This is equivalent to examine the contribution in each model and then average the contributions over the models because of the linearity in the averaging.

To attribute changes in the top-10-cm and total SM, surface and total R, and E, Zhao and Dai (2015) considered precipitation as the primary driver because it is determined mostly by atmospheric processes that are largely independent of local E and R. However, it is difficult to accurately quantify the contributions from individual drivers because of the intercorrelations among these variables. Here, the attribution to each driver is estimated approximately using the surface water balance equation: $d\mathrm{SM}/dt = P - E - R$. Zhao and Dai (2015) used a progressive regression method to estimate the contributions from individual drivers to the future changes for the top-10-cm SM, total R, and E. It seems that the future changes, especially in top-10-cm SM, were attributed more to the P than the E changes based on this method. In this study, we utilized a similar but more physically sound method to attribute the changes in surface and total SM, surface and total R, and E to individual drivers, with the following equations based on water-balance considerations:

$$\Delta \mathrm{SM} = a_1 \Delta P - b_1 \Delta E - c_1 \Delta R, \tag{1}$$

$$\Delta R = a_2 \Delta P - b_2 \Delta E, \tag{2}$$

$$\Delta E = a_3 \Delta \mathrm{PET} + b_3 \Delta \mathrm{SM}_t, \tag{3}$$

where Δ denotes the change from 1970–99 to 2070–99 expressed in percent of the CMIP6 MMM for 1970–99. The attribution was done separately for each model run, and then the attributed change was averaged over all models to derive the attributed change shown in Figs. 11–15. Equation (1) assumes that soil water storage increases with P, but decreases with E and R; Eq. (2) says R increases with P but decreases with E, with the effect of ΔSM being ignored in Eq. (2) as it is small compared with the

Brought to you by SUNY ALBANY LIBR SB23 | Unauthenticated | Downloaded 01/06/22 06:58 PM UTC

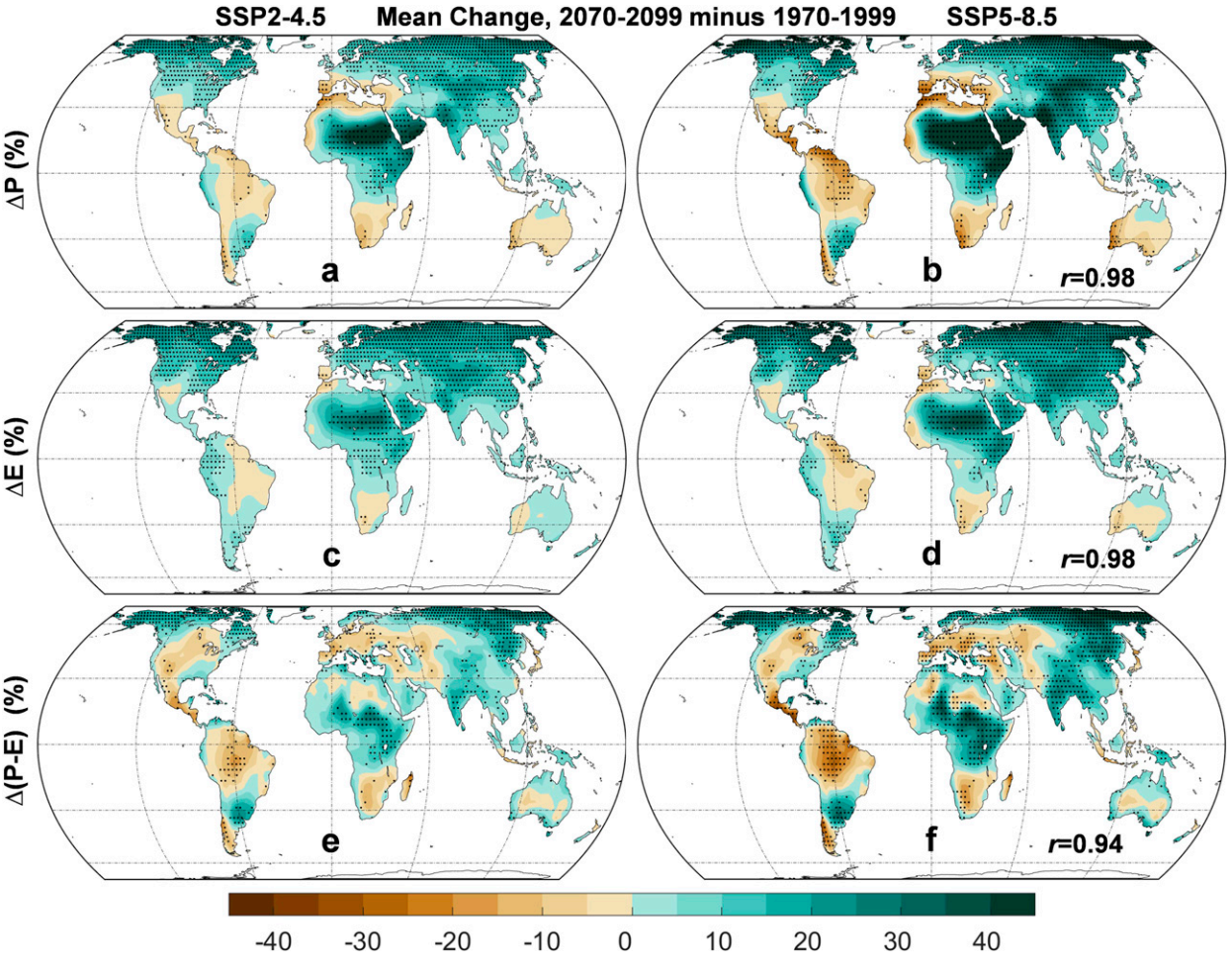

FIG. 1. CMIP6 multimodel ensemble mean changes (in % of the MMM for 1979–99) from 1970–99 to 2070–99 under the (left) SSP2-4.5 and (right) SSP5-8.5 scenario for annual land (a),(b) precipitation (ΔP); (c),(d) evapotranspiration (ΔE); and (e),(f) their differences [$\Delta(P - E)$] averaged over 25 CMIP6 models. The $\Delta(P - E)$ is comparable with the total R change (Figs. 2g,h) with a pattern correlations of 0.75 and 0.80 under the two scenarios. The stippling indicates at least 80% of the models agree on the sign of change. The pattern correlation (r) between the two scenarios is also shown in the right panels.

P and E flux changes integrated over a 30-yr period (which is supported by the similarity between the model-projected R and $P - E$ changes; cf. Figs. 1e,f and 2g,h). Equation (3) assumes that the E change is positively driven by PET (atmospheric demand) and total SM (SM_t, water supply) changes. Tests showed that adding surface SM to Eq. (3) made little difference because of their similar change patterns (Fig. 2). The a_1, b_1, c_1; a_2, b_2; and a_3, b_3 coefficients were determined through iterations at each grid box: each of them was allowed to vary independently from 0.0 to 1.0 with an interval of 0.05 [e.g., this yielded $21 \times 21 \times 21 \approx 9.3 \times 10^3$ combinations for Eq. (1)], the resultant changes for SM, R and E were compared with those projected by the CMIP6 models, and the combination of the coefficients that yielded the minimum deviation from the CMIP6 model-projected change was chosen as the best fit and used to attribute the contributions from the changes in individual drivers. Except for the iterative procedure, Eqs. (2) and (3) for the (surface and total) R and E used here are similar to those of Zhao and Dai (2015). Because of the use of the minimum deviation at each grid box, the attributed changes are more comparable with the model-projected changes with higher pattern correlations than those in Zhao and Dai (2015).

We realize that SM can cause variations in P, E, or R, so that some of the variations in P, E, or R is an effect, not a cause, of the SM variations. This suggests that Eq. (1) may overestimate the contributions of the P, E, or R to SM's variations if it were applied to their year-to-year variations. The same issue may also exist for the long-term changes among them; that is, some of the future changes in P, E, or R may be a result, rather than a cause, of the SM change. The issue also applies to Eq. (3), as the E change could affect the SM change; however, the R change should have little impact on the P or E changes in Eq. (2). This suggests that such an approach may overestimate the contributions from the drivers for the SM and E changes. However, the use of the minimum deviation in our

Brought to you by SUNY ALBANY LIBR SB23 | Unauthenticated | Downloaded 01/06/22 06:58 PM UTC

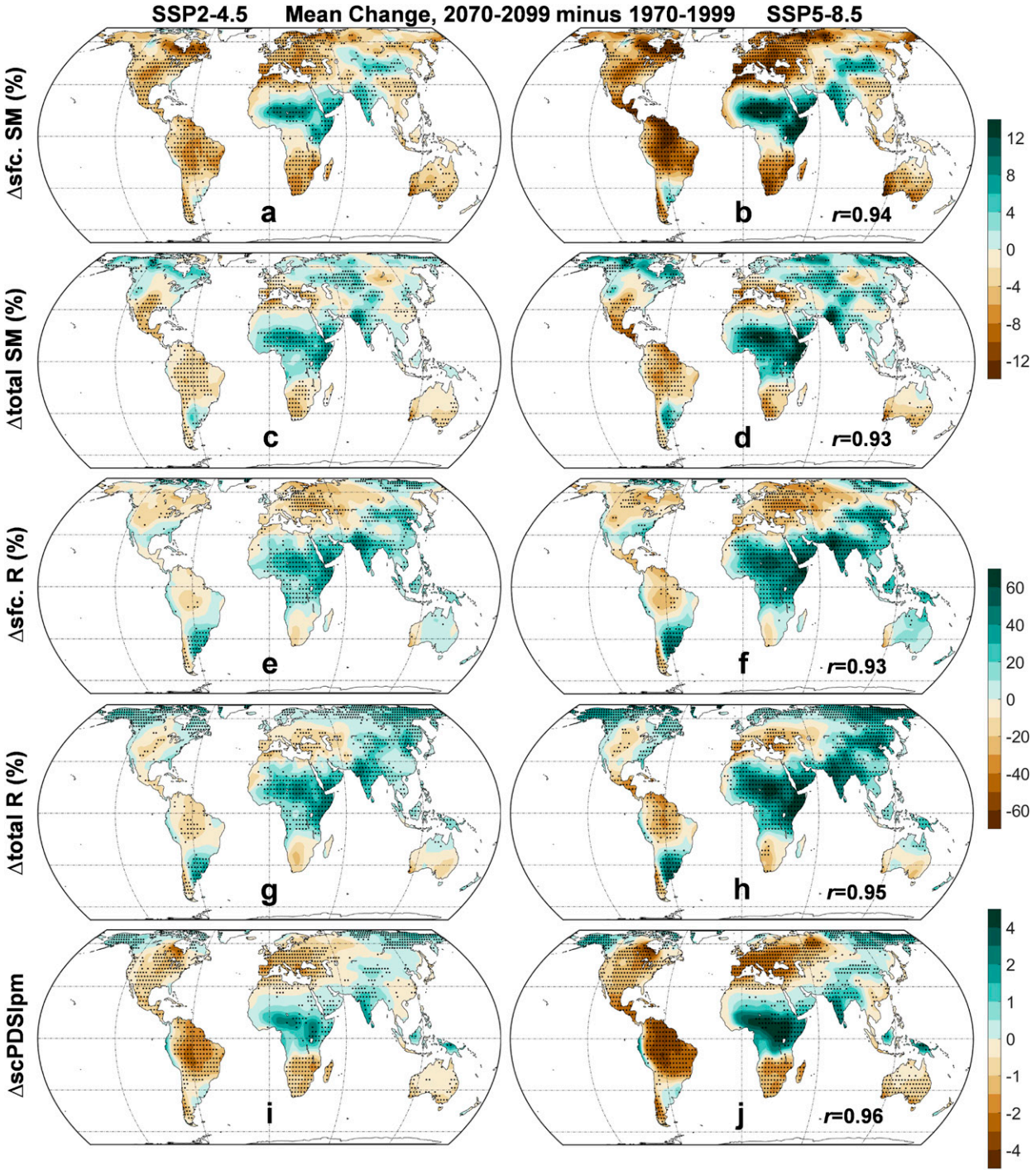

FIG. 2. CMIP6 multimodel ensemble mean changes (in % of the MMM for 1979–99) from 1970–99 to 2070–99 under the (left) SSP2-4.5 and (right) SSP5-8.5 scenario for annual (a),(b) top-10-cm soil moisture (SM); (c),(d) total SM; (e),(f) surface runoff (R); (g),(h) total R; and (i),(j) scPDSIpm. The scPDSIpm was computed for each model and averaged over 25 CMIP6 models, of which only 22 models had data for top-10-cm SM, 23 for total SM, 23 for surface R, and 24 for total R that were used in the ensemble averaging in this and other figures. All changes are in % of the MMM for 1970–99, except for scPDSIpm, which is in absolute change. Note a scPDSIpm value below −3 is considered as severe drought for today's climate. The stippling indicates at least 80% of the models agree on the sign of change. The pattern correlation (r) between the two scenarios is also shown in the right panels.

Brought to you by SUNY ALBANY LIBR SB23 | Unauthenticated | Downloaded 01/06/22 06:58 PM UTC

iterations to derive the coefficients in Eqs. (1)–(3) should minimize this overestimation of the contributions. Given that it is difficult to separate such interdependence among these coupled fields, and that the attributed changes by Eqs. (1)–(3) generally match the model-projected changes quite well with little overestimation, we used Eqs. (1)–(3) to make an approximate attribution of the projected changes in SM, R, and E to the changes in the other physically related variables, while recognizing the limitations of this analysis.

3. Hydroclimatic and drought changes

As pointed out by Cook et al. (2020), strong warming is evident across the twenty-first century in the CMIP6 model simulations (see Fig. S1 in the online supplemental material). The warming differs among the two scenarios; even within the same scenario, the spread increases with time, with a median warming of 3.0 and 4.9 K under the SSP2-4.5 and SSP5-8.6 scenario, respectively, in the late twenty-first century (2070–99) relative to the 1851–80 mean. The large spreads across model simulations result in significant overlap between the two scenarios.

a. *Hydroclimatic mean changes*

Before we examine the drought changes, which represent changes in dry *extremes*, we first briefly discuss the *mean* changes in major hydroclimatic fields from 1970–99 to 2070–99. Annual P is projected to increase by 10%–30% under SSP2-4.5 across many land areas over Eurasia, North America, central and northern Africa, and southeastern South America, with larger increases (up to 40%–60%) under SSP5-8.5 (Figs. 1a,b). In contrast, annual P declines (by 5%–10% under SSP2-4.5 and up to 30% under SSP5-8.5 in southwest North America, Central America, central to northern South America, the Mediterranean region, southern Africa, and Australia. These drying land regions are part of the larger subtropical drying zones that extend to the oceans (Collins et al. 2013; Dai 2021) and are likely caused by several factors (Dai et al. 2018), including increased drying by subsidence due to increased vertical gradients of specific humidity (Chou et al. 2009), increased vertical motion (Dai et al. 2018), and expansion of the subtropical drying zones (Lu et al. 2007; Scheff and Frierson 2012). Except for a larger magnitude under the SSP5-8.5 scenario, the P change patterns under both emissions scenarios are highly consistent (Figs. 1a,b). They are also roughly consistent with the results seen in previous CMIP3 and CMIP5 models (e.g., Hoerling et al. 2012; Knutti and Sedlacek 2013; Seth et al. 2013; Lee and Wang 2014; Zhao and Dai 2015; Ting et al. 2018; Seager et al. 2019; Dai 2021), although there are some uncertainties regarding the sign of the P change over northern Australia and a few other transition zones. The large P increases over East Africa appear to be part of a large zone with increasing rainfall associated with enhanced moist convection in the intertropical convergence zone (ITCZ) from Africa to the Indian Ocean, while the large percentage increase over northern Africa is partly due to the low climatological P there.

The pattern and magnitude of the E change under both scenarios (Figs. 1c,d) closely follow those of the P change (Figs. 1a–d), and they are very similar to those projected by CMIP5 models (Collins et al. 2013; Zhao and Dai 2015). The change of the precipitation minus evaporation [i.e., $\Delta(P - E)$] flux (Figs. 1e,f) suggests decreased runoff (by 5%–30%) largely over areas with P decreases but with more widespread decreases in North America, Europe, and western Asia. Such spatial pattern and magnitude in $\Delta(P - E)$ mainly reflect the changes in total R (Figs. 2g,h, with pattern correlations of 0.75 and 0.80 under SSP2-4.5 and SSP5-8.5, respectively) rather than changes in surface R. Elsewhere, annual runoff changes (Figs. 2e–h) are closely tied to annual P changes, as noticed previously (Cook et al. 2020).

Driven by large PET increases (Zhao and Dai 2015), surface (top 10 cm) SM (Figs. 2a,b) displays widespread drying by 4%–10% (5%–15%) under SSP2-4.5 (SSP5-8.5) over most land areas, including Europe, the Americas, Southeast and northern Asia, Australia, and southern Africa. Only East Africa, parts of northern Africa, the Middle East, central Asia, and India see significantly increases in surface SM. In contrast, total SM (Figs. 2c,d) shows less widespread drying than surface SM, with decreases mainly over most South America (except its southeast), Central America, southern North America, the Mediterranean region, southern Africa, and most Australia. As atmospheric demand for moisture directly affects surface soil moisture, it is expected that increases in PET would have a larger drying effect on the surface layer than on subsurface layers. It may also reflect reduced sensitivity of deeper SM to increased evaporative demand because of stronger controls on subsurface SM by vegetation processes (e.g., increased water use efficiency under higher atmospheric CO_2 levels) (Swann et al. 2016; Berg et al. 2017), although the role of rising CO_2's effect on plants is found to be small in a recent study by Scheff et al. (2021).

On a long-term (e.g., 30-yr mean) basis, total R is close to $P - E$ as land water storage changes are relatively small compared with the 30-yr integrated flux changes (Trenberth et al. 2007). This leads to their similar change pattern and magnitude (cf. Figs. 2g,h and 1e,f), with large increases (10%–40% under SSP2-4.5 and 20%–60% under SSP5-8.5) over most Asia and Africa (except southern Africa), northern Europe, Alaska, and southeast South America. In contrast, surface runoff shows more widespread decreases over Europe and western Asia, most North America (except its southern part), but increases over most Australia (Figs. 2e,f). The inconsistent between the regional changes in surface and total R and between P and R changes indicate that annual precipitation changes do not directly translate into R changes for many regions, where E, SM, or precipitation frequency changes also matter for R changes. The total R change patterns are broadly comparable to those seen in CMIP5 models (Collins et al. 2013; Zhao and Dai 2015), while surface R was not examined closely in previous studies.

The scPDSIpm change patterns (Figs. 2i,j) generally follow those for surface SM (Figs. 2a,b), except for northern Asia and Alaska. The scPDSIpm suggests drier future conditions

Brought to you by SUNY ALBANY LIBR SB23 | Unauthenticated | Downloaded 01/06/22 06:58 PM UTC

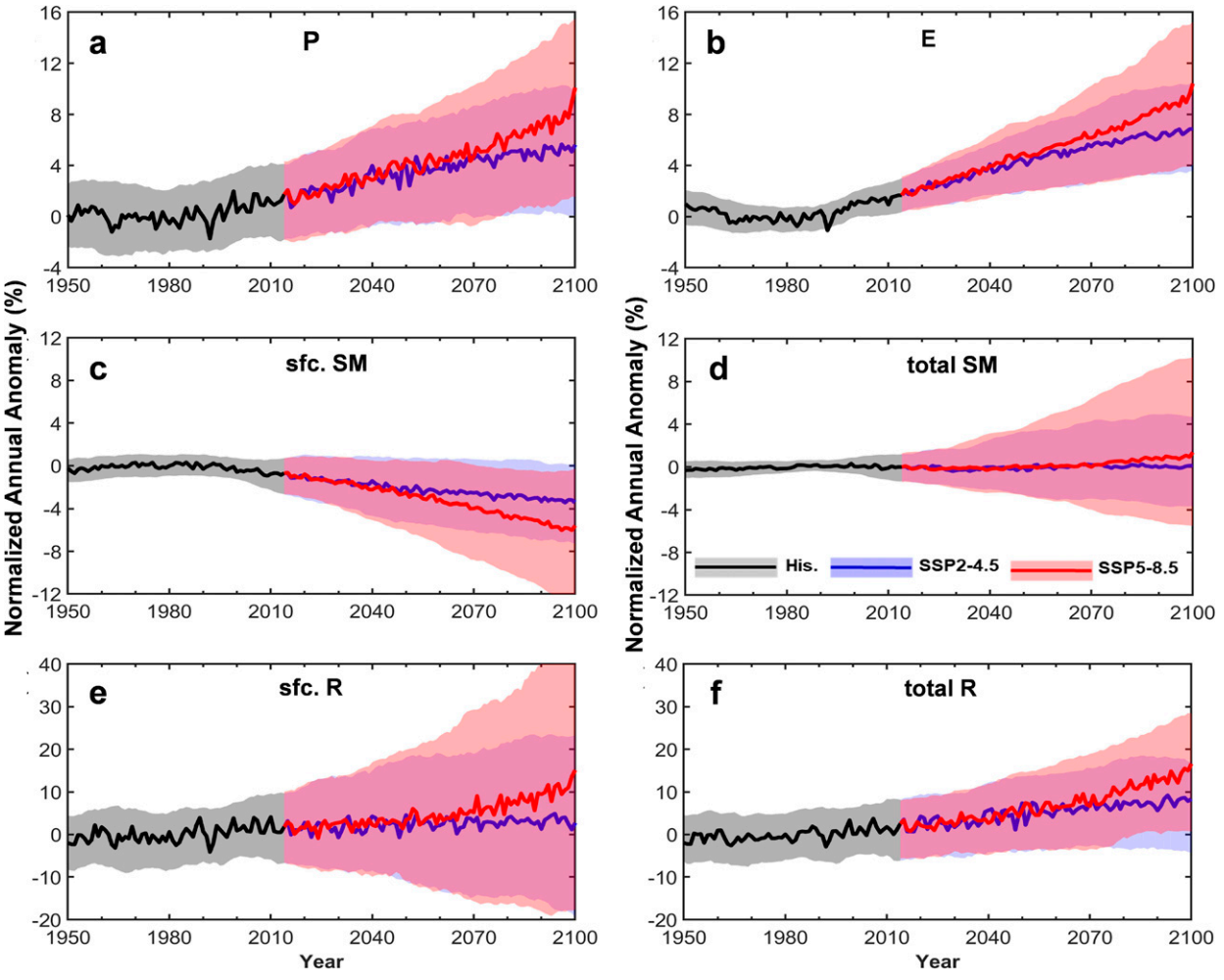

FIG. 3. CMIP6 multimodel ensemble-mean time series of normalized annual changes (relative to and in percentage of the 1970–99 mean) for (a) precipitation (P), (b) evaporation (E), (c) top-10-cm soil moisture (SM), (d) total SM, (e) surface runoff (R), and (f) total R averaged over global land (60°S–75°N). The shaded areas indicate the 10th–90th-percentile ranges (11-yr moving averages) of the changes among individual models during 1950–2014 (light gray) and 2015–2100 (light red/blue for SSP2-4.5, and light blue/red for SSP5-8.5), respectively.

over most of the Americas, Europe, southern Africa, Australia, and Southeast Asia. The drying over Southeast Asia is seen in both surface SM and scPDSIpm, even though precipitation increases there (in all seasons, Dai 2021), presumably most of the P increase led to R increases rather than increases in surface SW. These scPDSIpm change patterns are comparable to those seen in CMIP3 (Dai 2013a; Zhao and Dai 2017) and CMIP5 models (Zhao and Dai 2015, 2017).

Averaged over global (60°S–75°N) land areas, the ensemble-mean P, E, and (surface and total) R (Fig. 3) all show similar percentage increases of 4%–5% (10%–15%), while the surface SM decreases by about 3% (5%) by the end of the twenty-first century under the SSP2-4.5 (SSP5-8.5) scenario. In contrast, the total SM does not change significantly over the twenty-first century (Fig. 3d). Figures 3a and 3b further shows that the variations and long-term changes of the global-mean land P and E are highly consistent with each other under both scenarios (with a correlation of ~0.99 with trends and 0.79 and 0.88 after linear detrending during 1950–2100 under the two scenarios), suggesting that land E is controlled mainly by P. Large spreads exist among the individual model simulations even within a given scenario as pointed out by Cook et al. (2020), and the spread is especially large in the SM and R changes under SSP5-8.5. The very large spread in the normalized surface R is partly due to its small 1970–99 mean value used in the normalization. The spreads represent uncertainties associated with the forced response to future forcing and the effect of internal variability in individual simulations.

Largely consistent with Cook et al. (2020), drought responses to warming are highly season dependent, and the drought changes based on the drought metrics across most of the Northern Hemisphere midlatitudes are more severe and widespread in the warm season (April–September) than in the cold

Brought to you by SUNY ALBANY LIBR SB23 | Unauthenticated | Downloaded 01/06/22 06:58 PM UTC

season (October–March). In particular, the large drying in surface SM and R, and scPDSIpm in the warm season contributes the most to annual drought changes (see Figs. S2 and S3).

b. Changes in PDFs

Changes in the PDFs or their empirical estimates (i.e., histograms) are often used to quantify large changes in the frequency of extreme events resulting from a relatively small change in the PDF of a climate variable. Zhao and Dai (2015) showed that the histograms of the scPDSIpm, surface SM, and total R from 14 CMIP5 models are projected to flatten (besides a shift in the mean) over most land areas, with increased SDs and reduced peak frequency of occurrence. Cook et al. (2020) examined the robustness of the changes in the return frequency of meteorological, agricultural, and hydrological droughts based on 13 CMIP6 model simulations. Here, we analyze the simulations from 25 CMIP6 models to quantify the PDF changes for the scPDSIpm, surface and total SM, and surface and total R between the current (1970–99) and future (2070–99) periods. To ensure that the different annual-mean changes due to different climate sensitivities to future climate forcing among different models would not increase the spread of the future PDFs, we removed the annual-mean of the future period (2070–99) before computing the future PDFs for each model, and the PDFs were then averaged over all the models in Fig. 4. The standard deviation and peak frequency changes were similarly computed in Figs. 5 and 6 . In these calculations, the future change in the annual cycle is included. This is also the case for our calculations of the future drought events, which are based on the future anomalies relative to current monthly climatology.

Figure 4 shows the multimodel average of the PDFs estimated for individual model runs using monthly anomalies (relative to 1970–99 monthly climatology but with the future annual-mean removed) of the scPDSIpm, normalized surface and total SM and R over four selected regions (i.e., the western United States, southern Europe, southern Africa, and the Amazon) as outlined in Fig. 1a of Zhao and Dai (2015). The multimodel-ensemble mean PDFs largely follow Gaussian distributions, although they are non-Gaussian for some individual models (Figs. S5 and S6). In additional to a mean shift (mainly to the left, i.e., decrease), the future PDFs flatten under both scenarios (but more so under SSP5-8.5) with a reduced peak frequency and an increased spread for all the regions, especially for the Amazon and for total SM (Fig. 4). This implies a larger increase in total-SM-based drought (Figs. 4i,j) than that based on the other variables in these regions (consistent with Fig. 7). PDFs based on data from individual models (Figs. S4–S6) also show similar flattening. We have also investigated the PDFs changes for soil moisture and runoff from the 50 ensemble runs by CanESM5, and obtained similar results (Fig. S7). This suggests that the flattening and increased spread of the future PDFs are real and not due to our data processing. These PDF changes are consistent with those from the CMIP5 simulations reported by Zhao and Dai (2015), who did not analyze total SM and surface R.

Figures 5 and 6 further suggest that the PDF flattening for the drought indices are widespread and more severe under SSP5-8.5, with increased SD and reduced peak frequency of occurrence over global land (except southern Africa and a few other regions for the scPDSIpm case, similar for CMIP5, see Zhao and Dai 2015). The flattening is most pronounced over the northern high latitudes, northern Africa, and the Middle East for all the hydroclimatic fields. In particular, the SD and peak-frequency changes based on both surface and total R are especially large, although this is not evident for the four regions shown in Fig. 4.

Our calculations showed that the PDF flattening revealed by Figs. 4–6 results, to a large extent, from the future change in the mean annual cycle, as the flattening weakens or disappears when the future change in the mean annual cycle is excluded by removing the future monthly climatology from the data before computing the PDFs, SD, and peak frequency (Figs. S8–S10), although significant flattening still exists in the PDFs for surface and total runoff even after the removal of the future mean annual cycle. The normalized soil moisture and runoff decreases more in July than January over most of the northern latitudes and central-northern Africa; while the scPDSIpm decreases more July than January over most South America, central-southern Africa, Australia, the Pacific coasts of North America, the Middle East, and the Mediterranean region, and shows opposite changes over central-eastern Asia, northern Africa, northern South America, and central North America (Fig. S11). Since future drought events are defined using anomalies relative to current monthly climatology, the future change in the mean annual cycle is relevant for drought changes and thus should be included in the PDF analyses. Systematic flattening of the PDFs, combined with a decrease in the mean, would lead to large increases in drought events, which are represented by the left tails of the PDFs shown in Fig. 4.

Chen et al. (2019) showed that the PDFs of daily surface air temperatures in the twenty-first century would flatten over most of the globe except for winter northern mid- to high latitudes, while the seasonal amplitude of the surface air temperatures would increase at low latitudes but decrease at high latitudes. These PDF and seasonal changes at northern high latitudes are related to reduced variability associated with decreased sea ice variability and meridional thermal advection (Dai and Deng 2021). However, it is unclear whether and how these temperature changes are related to the hydroclimatic distribution changes shown in Figs. 4–6.

c. Changes in drought frequency, duration, and area

Figure 7 shows the drought frequency changes from 1970–99 to 2070–99 based on five drought measures. It is clear that the spatial pattern and magnitude of the drought frequency changes are broadly comparable among the estimates based on scPDSIpm, surface and total SM, with widespread increases (by 25%–100% under SSP2-4.5 and 50%–200% under SSP5-8.5) over the Americas, Europe, southern and northern Africa, Australia, and most of Asia (Figs. 7a–f), while the R-based estimates show widespread decreases in

Brought to you by SUNY ALBANY LIBR SB23 | Unauthenticated | Downloaded 01/06/22 06:58 PM UTC

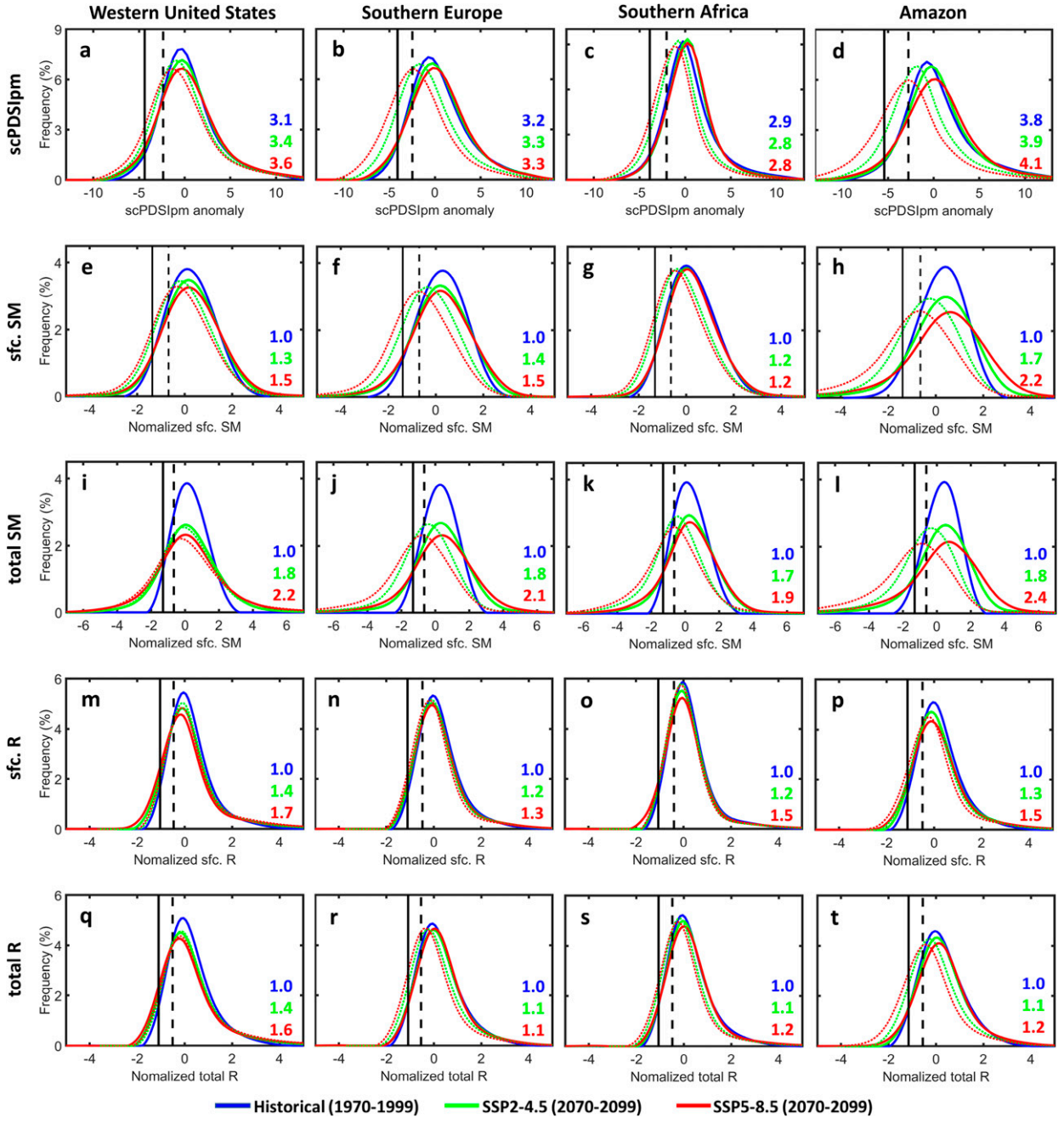

FIG. 4. Multimodel ensemble averages of the PDFs from individual models derived by spline-fitting the histograms of the occurrence frequency estimated using local monthly anomalies (relative to the 1970–99 monthly climatology and with the future annual mean removed) from all grid cells within each region from individual model runs during 1970–99 (blue) and 2070–99 under the SSP2-4.5 (green) and SSP5-8.5 (red) scenario for (a)–(d) scPDSIpm; (e)–(h) top-10-cm soil moisture; (i)–(l) total soil moisture; (m)–(p) surface runoff; and (q)–(t) total runoff over (a),(e),(i),(m),(q) the western United States; (b),(f),(j),(n),(r) southern Europe; (c),(g),(k),(o),(s) southern Africa; and (d),(h),(l),(p),(t) the Amazon. The solid (dashed) colored lines represent the future PDFs without (with) the future annual-mean change (estimated separately from the mean change and then added to the solid lines to derive the dashed lines). The monthly anomalies for both periods of the soil moisture and runoff were normalized at each grid box to be in units of the SD of the 1970–99 period before estimating the PDFs. The colored numbers on each panel are the SD of the PDFs for 1970–99 (blue) and 2070–299 under the SSP2-4.5 (green) and SSP5-8.5 (red) scenario. The vertical black solid (dashed) lines are the 10th (20th) percentile of the historical PDF. Student's *t* test and *F* test indicate the future changes in the mean and variance of the PDFs are significant at the 5% level for all the cases.

Brought to you by SUNY ALBANY LIBR SB23 | Unauthenticated | Downloaded 01/06/22 06:58 PM UTC

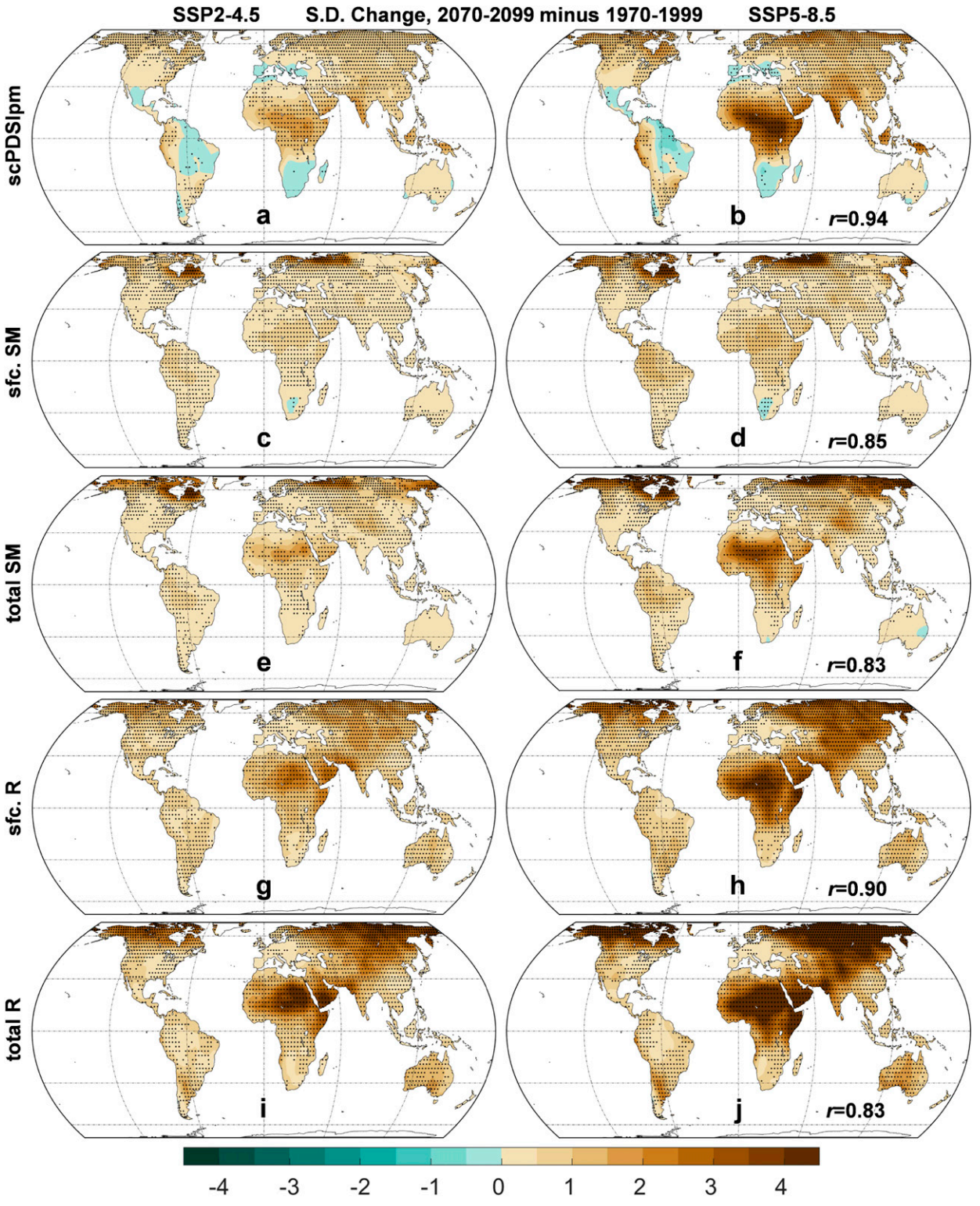

FIG. 5. CMIP6 multimodel ensemble mean changes from 1970–99 to 2070–99 under the (left) SSP2-4.5 and (right) SSP5-8.5 scenario in the SD of (a),(b) scPDSIpm; normalized (c),(d) top-10-cm and (e),(f) total soil moisture; and normalized (g),(h) surface and (i),(j) total runoff. The SD changes were first calculated for each model in units of the 1970–99 SD and then averaged over all the models. The pattern correlation (r) between the two scenarios is also shown in the right panels. The stippling indicates at least 80% of the models agreeing on the sign of change.

Brought to you by SUNY ALBANY LIBR SB23 | Unauthenticated | Downloaded 01/06/22 06:58 PM UTC

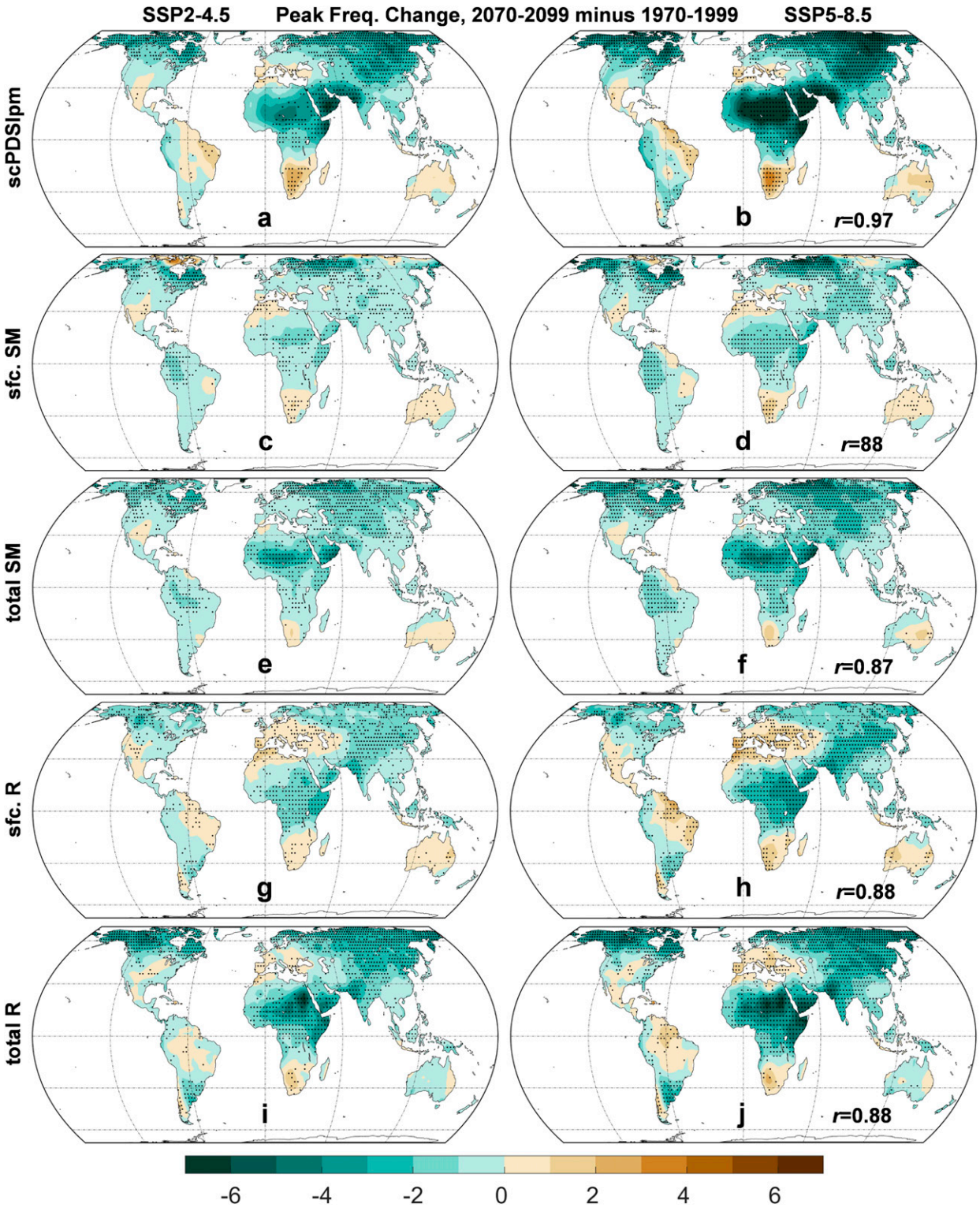

FIG. 6. CMIP6 multimodel ensemble mean changes from 1970–99 to 2070–99 in the peak frequency (in % of time) of the histograms of monthly anomalies under the (left) SSP2-4.5 and (right) SSP5-8.5 scenario for (a),(b) scPDSIpm; (c),(d) top-10-cm soil moisture; (e),(f) total soil moisture; (g),(h) surface runoff; and (i),(j) total runoff. The peak frequency was first estimated for each model based on the local PDFs derived using cubic spine fitting to the local histograms over the 30-yr periods and then averaged over all the models. The pattern correlation (r) between the two scenarios is also shown in the right panels. The stippling indicates at least 80% of the models agreeing on the sign of change.

Brought to you by SUNY ALBANY LIBR SB23 | Unauthenticated | Downloaded 01/06/22 06:58 PM UTC

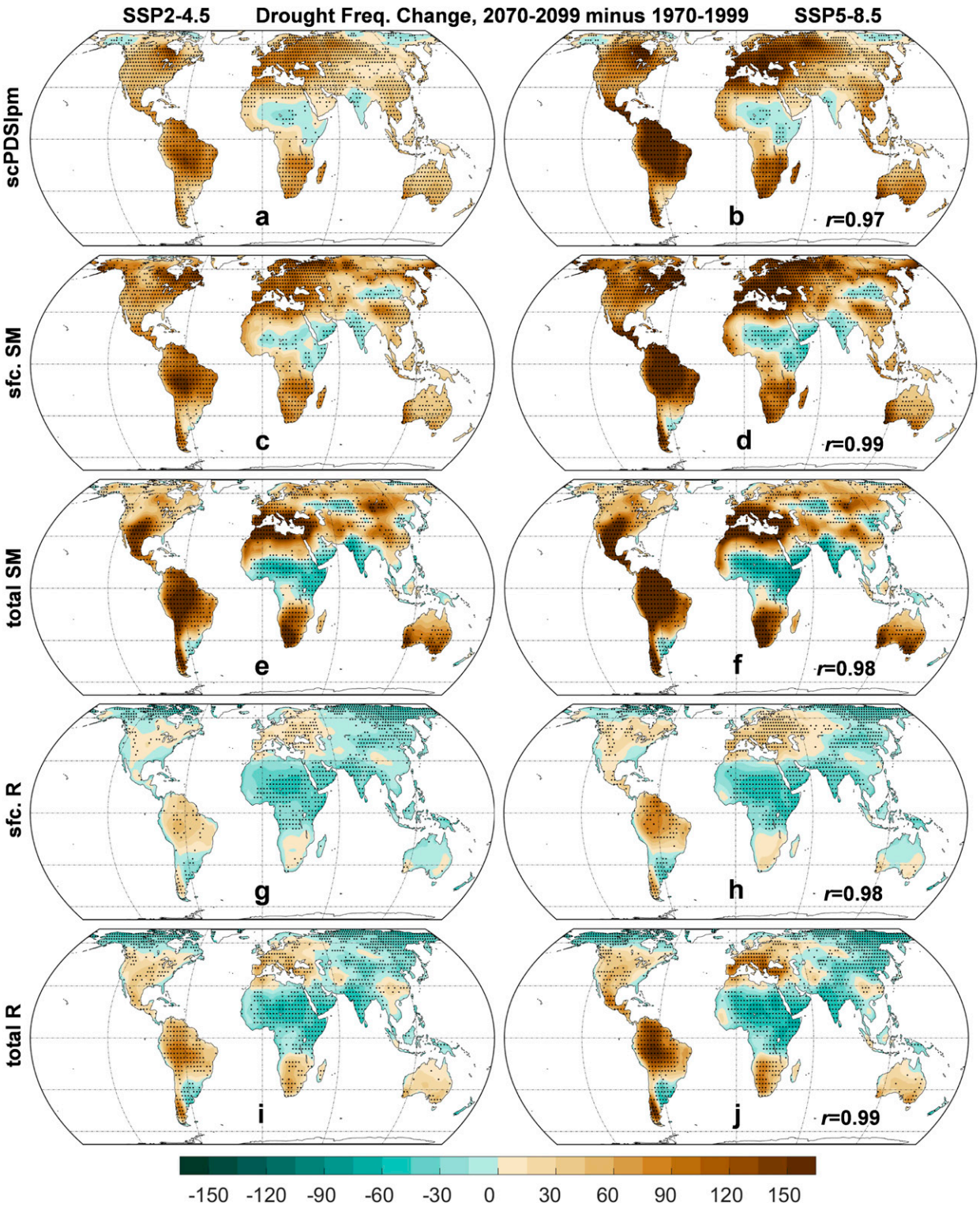

FIG. 7. CMIP6 multimodel ensemble mean changes (in % of the MMM for 1979–99) from 1970–99 to 2070–99 in the drought frequency under the (left) SSP2-4.5 and (right) SSP5-8.5 scenario, with drought defined locally as months with an anomaly (relative to 1979–99 monthly climatology) below the 20th percentile of the 1970–99 period based on (a),(b) scPDSIpm; (c),(d) normalized top-10-cm soil moisture [i.e., in units of STD of 1970–99, same for (e)–(j)]; (e),(f) normalized total soil moisture; (g),(h) normalized surface runoff; and (i),(j) normalized total runoff from individual model runs. The drought frequency change was calculated for each model run first and then averaged over all the models to derive the ensemble mean change shown here. The pattern correlation (r) between the two scenarios is also shown in the right panels. The stippling indicates at least 80% of the models agreeing on the sign of change.

Brought to you by SUNY ALBANY LIBR SB23 | Unauthenticated | Downloaded 01/06/22 06:58 PM UTC

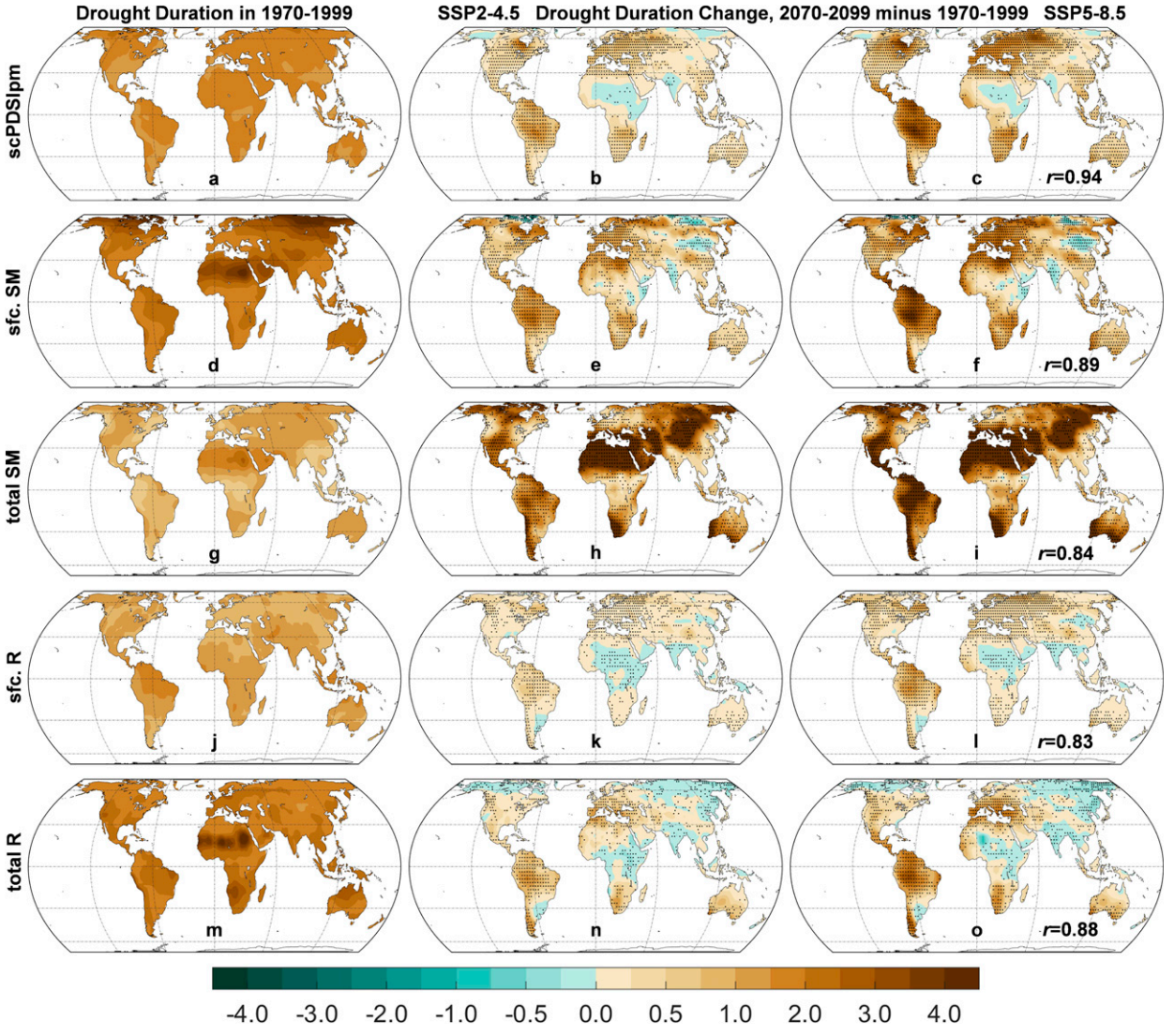

FIG. 8. CMIP6 multimodel ensemble mean of the drought duration (month) for the (left) historical period (1970–79) and the duration changes from 1970–99 to 2070–99 under the (central) SSP2-4.5 and (right) SSP5-8.5 scenario based on monthly anomalies (relative to the 1970–99 mean) of (a)–(c) scPDSIpm; (d)–(f) normalized top-10-cm SM; (g)–(i) normalized total SM; (j)–(l) normalized surface R; and (m)–(p) normalized total R from individual model runs. The drought duration is defined locally as a period of consecutive months with the monthly anomalies below the 20th percentile of the 1970–99 period. The mean duration and its change were calculated for each model run first and then averaged over all the models to derive the ensemble mean shown here. The pattern correlation (r) between the two scenarios is also shown in the right panels. The stippling indicates at least 80% of the models agreeing on the sign of change. Note the duration and duration changes for total SM in (g)–(i) are multiplied by a factor of 0.2 in order to use the same color bar.

drought frequency over Asia and central-northern Africa (Figs. 7g–j). Figures 7a and 7c are comparable to Figs. 8b and 8d of Zhao and Dai (2015) derived from CMIP5 models using similar measures, except that the CMIP6 results show more decreases over east-central Africa, the Arabian and Indian Peninsulas, and the scPDSIpm from CMIP5 models show decreased drought frequency over northern northeastern Asia, Alaska, and northern Canada. In particular, the total SM-based drought frequency increases more than that based on surface SM over South America, Central America, southwest North America, the Mediterranean region, southern Africa, and Australia (Figs. 7c–f), even though the mean of total SM decreases less than surface SM over these regions (Fig. 2). This results from the larger PDF flattening in total SM than in surface SM (Figs. 4–6), and shows that a smaller decrease in total SM, as reportedly by Berg et al. (2017), does not necessarily mean fewer droughts. The drought frequency based on the normalized surface and total R shows similar change patterns with relatively small changes (within ±5% under SSP2-4.5 and ±5%–20% under SSP5-85) over most

Brought to you by SUNY ALBANY LIBR SB23 | Unauthenticated | Downloaded 01/06/22 06:58 PM UTC

land areas with increased frequency over most South America, and the change patterns generally follow the mean changes in R (Figs. 2e–h). In contrast, the CMIP5 models (Fig. 8f of Zhao and Dai 2015) show more widespread increases in total R-based drought frequency over Africa and Asia. In general, the increases in drought frequency in the twenty-first century based on the scPDSI, SM, and R all are robust across many drying regions, including most North America (except its high latitudes), Central and South America (except southeast South America), Europe and the Mediterranean region, southern Africa, Australia, and most of Asia (except India, the southern Arabian Peninsula, and the R-based cases). These results largely confirm the findings of Cook et al. (2020), and are roughly consistent with those from the CMIP5 model simulations (Zhao and Dai 2015), except that our SM-based drought increases are more widespread than those for extreme drought events shown by Cook et al. (2020) and that our R-based drought frequency shows more widespread decreases over central and northern Africa and Asia than those from the CMIP5 models (Zhao and Dai 2015).

Figure 8 shows that the change patterns in drought duration are very similar to those for drought frequency, with increased duration (by 0.2–3.0 months under SSP2-4.5 and 0.5–5.0 months under SSP5-8.5 based on scPDSIpm or surface SM) over most of the America, Europe, the Mediterranean region, southern Africa, Australia, and most Asia (except for India and the southern Arabian Peninsula for the SM case). This is expected because by definition the drought duration (D) is related to drought frequency (F): $D = F \times T/N$, where T is the time period examined and N is the number of separate drought events within this period. Nevertheless, the duration change still provides helpful information as it shows on average how much longer future drought events will become. Similar to the frequency change, the R-based duration increases are smaller and less widespread than those based on the scPDSIpm and SM. The duration increases based on total SM are particularly large (by 10+ months) over many of the drying regions (Figs. 8h–i).

For global land (60°S–75°N) as a whole, the percentage area under drought conditions based on the scPDSIpm is projected to increase from 20% to about 28% (35%) under the SSP2-4.5 (SSP5-8.5) scenario from 1950 to 2100, along with the increases in areas under agricultural droughts defined by the normalized SM to 30%–35% (33%–39%) for SSP2-4.5 (SSP5-8.5) with surface SM indicating the largest increase (Figs. 9a,b). The areas under hydrological drought increase only slightly, from ~20% to ~25%–26% under SSP5-8.5 (Fig. 9b); this is especially true for the Southern Hemisphere warm season (Figs. 9e,f). In contrast, the Northern Hemisphere warm season sees larger increases in the areas under drought than for the global mean and annual mean (Figs. 9a–d). Furthermore, drought areas seem to be more stabilized after about 2060s under SSP2-4.5 than SSP5-8.5 over global land and the Northern Hemisphere, as atmospheric CO_2 is stabilized after about 2060 under SSP2-4.5 (Meinshausen et al. 2020). Besides the relatively larger magnitude under the higher emissions scenario SSP5-8.5, the temporal evolution of the drought areas under SSP2-4.5 from the 25 CMIP6 models are broadly consistent with those under the RCP4.5 scenario from 14 CMIP5 models (Zhao and Dai 2015). This is, in part, because the SSP2-4.5 scenario is closely comparable to the RCP4.5 scenario that stabilizes at ~4 W m^{-2} after about 2065 (van Vuuren et al. 2011). The drought area changes based on scPDSIpm are also largely consistent with those from 12 CMIP3 model simulations under the moderate A1B scenario (Zhao and Dai 2017).

The above results overall suggest that the spatial patterns of the drought changes from 1970–99 to 2070–99 based on the scPDSIpm and normalized surface and total SM anomalies are broadly comparable with increased drought frequency over most land areas except central-eastern Africa, India, and a few other regions, and with noticeable differences in their change magnitude especially under SSP5-8.5. On the other hand, the R-based drought changes show smaller magnitudes and more widespread decreases in drought frequency over central-northern Africa and Asia than the scPDSIpm and SM-based estimates and the CMIP5 models (Zhao and Dai 2015). The increases in drought frequency, duration, and areas are largest for the normalized surface SM-based agricultural drought, closely followed by those based on the total SM and scPDSIpm, while those for R-based hydrological drought change little in the twenty-first century. The differences of the agricultural and hydrological drought changes between the CMIP6 and CMIP5 models (e.g., Zhao and Dai 2015) result mainly from their differences in precipitation changes, especially over the margins of the subtropical regions (e.g., central-northern Africa, cf. our Figs. 1a,b and Fig. 1 of Zhao and Dai 2015). Our results largely reaffirm conclusions of Cook et al. (2018), who found that soil moisture and runoff-based drying in 13 CMIP6 models is more robust, spatially extensive, and severe than that based on precipitation, even in regions where precipitation responses are not robust. This is mainly due to the drying effect associated with rising surface temperatures, as well as the PDF flattening discussed above. We perform an attribution analysis to further reveal the contributions from individual factors to the projected hydroclimatic changes.

4. Attribution of the future hydroclimatic changes

a. Attribution of scPDSIpm changes

Figure 10 shows the individual contributions to the projected scPDSIpm change under SSP2-4.5 and SSP5-8.5 from changes in precipitation (P), near-surface air temperature and specific humidity ($T + q$), surface net longwave radiation (LW) and shortwave radiation (SW), and surface wind speed (WS). The sum (Figs. 10k,l) of the contributions from all the individual factors highly agrees with the projected changes with all factors included at the same time (Figs. 2i,j), with a pattern correlation of 0.96 under both scenarios. This suggests that our method to estimate the individual contributions works well. It is clear that the scPDSIpm change over most global land results mainly from changes in P and ($T + q$), followed by changes in SW, with small contributions from changes in LW and WS (Figs. 10e,f,i,j). Precipitation increases cause the scPDSIpm to increase by 1–2 (1–5) units under the SSP2-4.5 (SSP5-8.5) scenario over most of Eurasia, North America except its southwest, and central-northern Africa,

Brought to you by SUNY ALBANY LIBR SB23 | Unauthenticated | Downloaded 01/06/22 06:58 PM UTC

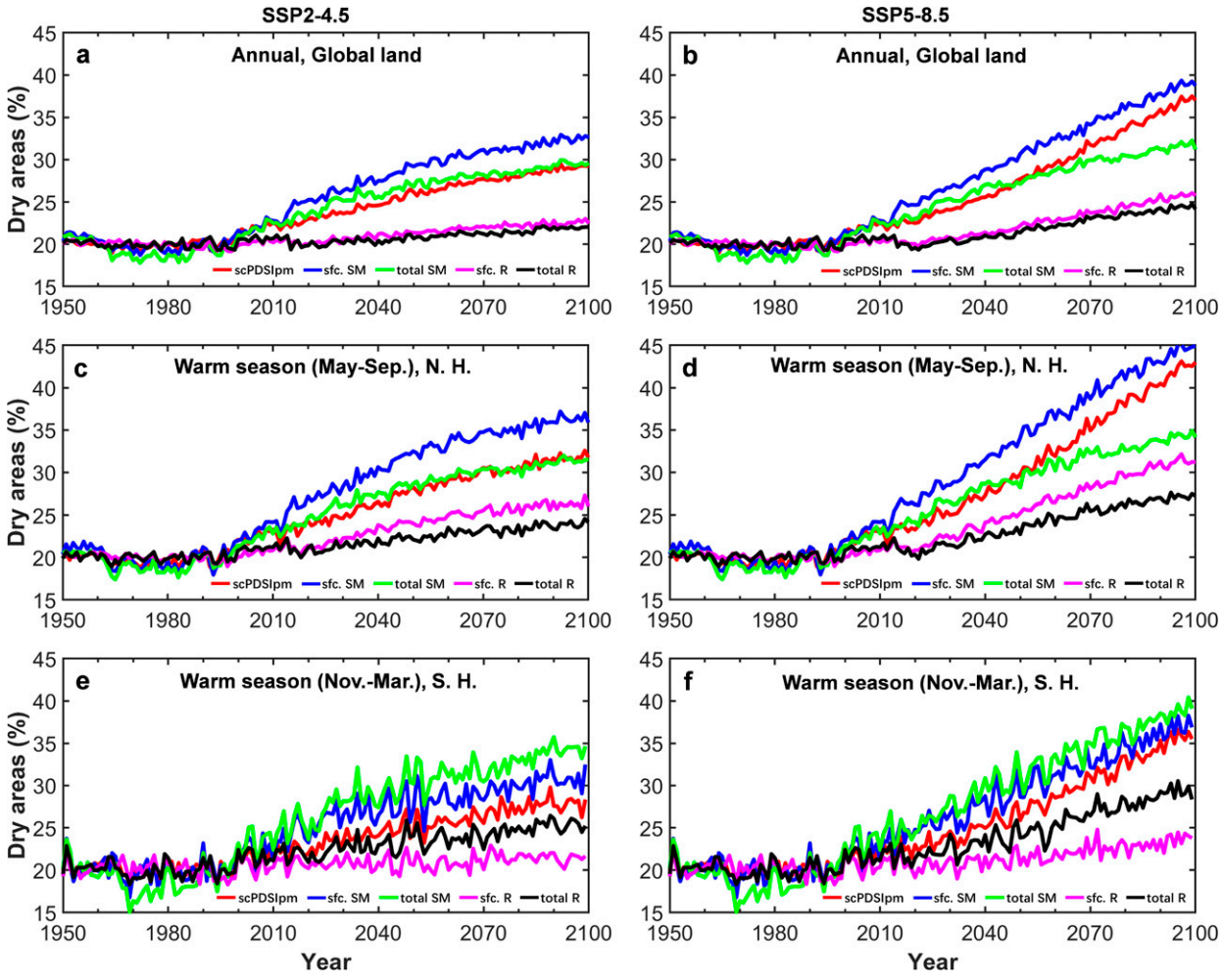

FIG. 9. Multimodel ensemble mean of the percentage changes in drought areas under the (left) SSP2-4.5 and (right) SSP5-8.5 scenario over (a),(b) global land area (in % of the total land area between 60°S and 75°N) for the annual mean; (c),(d) Northern Hemisphere land for warm season from May to September; and (e),(f) Southern Hemisphere land for the warm season from November–March. A drought event is defined at each grid as a month whose scPDSIpm, top-10-cm SM, total SM, surface R, or total R is below the 20th percentile of the 1970–99 period.

whereas P decreases lead to scPDSIpm decreases (i.e., drying) by about 0.5–1 (1–3) units over southwest North America, Central America, most of South America except its southeast, southern Africa, the Mediterranean region, and Australia (Figs. 10a,b). In contrast, surface warming and the associated increases in surface vapor pressure deficit (VPD) lead to ubiquitous decreases of scPDSIpm by 0.25–2.0 (0.5–3.0) units under SSP2-4.5 (SSP5-8.5), especially over the northern high latitudes and inland of South America (Figs. 10c,d). Changes in surface net SW has considerable drying effects over the northern high latitudes (Figs. 10g,h).

The total effects of these changes, primarily from P and $(T + q)$, result in drying over most of the Americas, Europe, southern Africa, and Australia (Figs. 10k,l). These drying patterns are consistent with those from CMIP5 models (Zhao and Dai 2015). While surface warming and the associated VPD cause widespread drying (Figs. 10c,d), the wetting effect from increased P offsets this drying over Asia, central-northern Africa, and Alaska, leading to severe drying mainly over the regions with decreasing precipitation (Figs. 10k,l).

b. *Attribution of surface and total soil moisture changes*

Figure 11 shows the changes (in % of the MMM for 1970–99) in top-10-cm-layer soil moisture (ΔSM) from 1970–99 to 2070–99 due to changes in precipitation (ΔP), evapotranspiration (ΔE), and surface runoff (ΔR) based on Eq. (1). Our previous study (Zhao and Dai 2015) attributed all the SM variance or changes associated with both P and E to P only (as P being considered as the primary driver). This may lead to overestimates of the contributions from ΔP. Compared with the CMIP5 results of Zhao and Dai (2015), increased E leads to more drying over many land areas in Eurasia, northern Africa, and North America in Fig. 11, which is more reasonable physically.

Brought to you by SUNY ALBANY LIBR SB23 | Unauthenticated | Downloaded 01/06/22 06:58 PM UTC

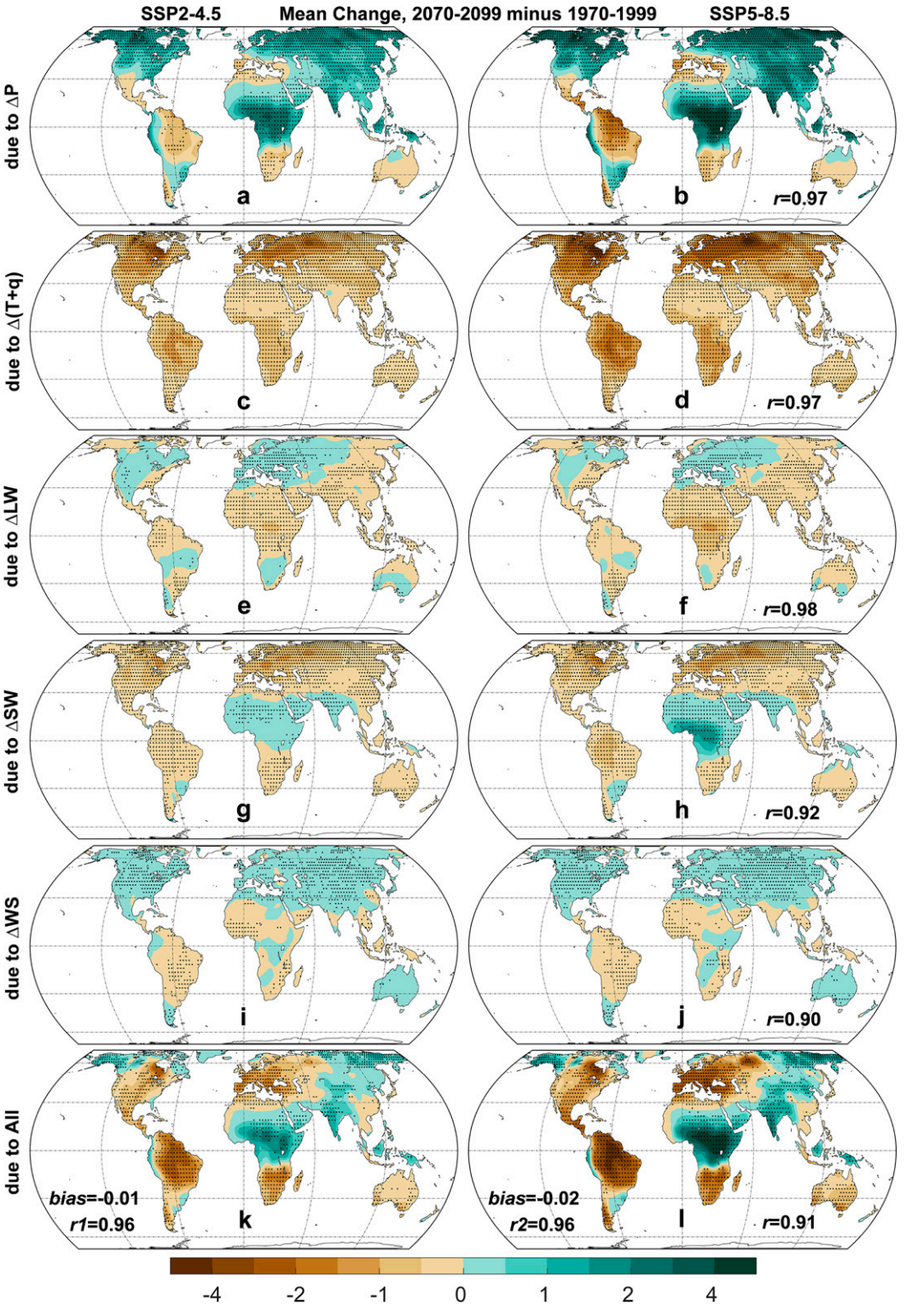

FIG. 10. Attribution of the annual scPDSIpm changes from 1970–99 to 2070–99 under the (left) SSP2-4.5 and (right) SSP5-8.5 scenario to changes in an individual factor with all other variables set to the mean value of 1970–79 for decades outside the calibration period (1950–79). The individual forcing cases were done for each model run and the 2070–99 minus 1970–99 difference was averaged over the models to derive the changes shown here. The individual drivers include changes in (a),(b) precipitation (ΔP); (c),(d) near-surface air temperature and specific humidity $[\Delta(T + q)]$; (e),(f) net surface longwave radiation (ΔLW); (g),(h) net surface shortwave radiation (ΔSW); and (i),(j) near-surface wind speed (ΔWS). (k),(l) The sum of the scPDSIpm changes induced by all the factors (All), which are comparable with the actual scPDSIpm change (Figs. 2i,j) with a pattern correlation (r1 and r2) of 0.96, as well as a global mean bias of −0.01 and −0.02 under both scenarios, respectively. The stippling indicates at least 80% of the models agreeing on the sign of change. The pattern correlation (r) between the two scenarios is also shown in the right panels.

Brought to you by SUNY ALBANY LIBR SB23 | Unauthenticated | Downloaded 01/06/22 06:58 PM UTC

Figure 11 shows that both ΔP and ΔE are important drivers of surface SM changes, with opposite effects over most land areas. The ΔP accounts for most of the surface SM decreases over the Mediterranean region, southern Africa, southwest North America to central South America, and Australia, while it increases SM over the rest of the world (especially over east-central Africa, India, and central Asia) that is partially offset by negative contributions from increased E (Figs. 11a–d). Increased surface R offsets some of the SM increases caused by increased P over east-central Africa and South Asia. The combined contributions from these factors (Figs. 11g,h) are comparable with the model-projected changes shown in Figs. 2a,b, with a pattern correlation of 0.97–0.98 and a slight positive mean bias of 0.4%–0.6%, which is the difference of the global mean between Figs. 11g,h and 2a,b.

For total soil moisture changes (Fig. 12), the contributions from the ΔP, ΔE, and total ΔR are roughly similar to their contributions to surface ΔSM, again with the largest and often opposite contributions from the P and E changes. The contributions from ΔR are relatively small, and both the drying and wetting magnitudes for total SM are smaller than those for surface SM (Figs. 11 and 12). The combined contributions (Figs. 12g,h) are also comparable to the model-projected changes (Figs. 2c,d), with a pattern correlation of 0.95–0.98 and a small negative mean bias of −0.2% to −0.3%.

c. *Attribution of surface and total runoff changes (ΔR)*

Although runoff changes are tied closely to precipitation changes, the negative impact of increased E on future runoff is nonnegligible (Zhao and Dai 2015). This is also true in our analysis here: Figs. 13 and 14 show that while increased P leads to more surface and total R over many land areas over Eurasia, Africa, and North America (except the subtropical drying regions), increased E offsets some of the R increases over these regions. The sum of their contributions is comparable to the model-projected runoff changes shown in Fig. 2, with a pattern correlation of ~0.94 and a negative global mean bias of −2% to −4%. Thus, our attribution method seems to work well.

d. *Attribution of evapotranspiration changes (ΔE)*

Evapotranspiration (E), a main component of the water cycle, is an important driver of agricultural and hydrological droughts. It is affected by atmospheric demand for moisture (often measured by PET) and water supply by soils (especially from top-layer soil moisture). Thus, we attribute E changes (ΔE) to changes in both PET and surface and total soil moisture, which seems to reproduce well the model-projected ΔE shown in Figs. 1c and 1d, with a pattern correlation of 0.91–0.92 and a negative mean bias of −3.4% to −4.5% (Figs. 15e,f). Figure 15 shows that increased PET associated with rising temperatures leads to ubiquitous E increases over land, especially over the northern high latitudes (by 20%–40%), while the SM changes lead to E reduction by 5%–20% over most of the Americas, southern Africa, Australia, Southeast Asia, Europe, and the Mediterranean region. Consistent with the CMIP5 results of Zhao and Dai (2015), Fig. 15 suggests a larger contribution from ΔPET changes than ΔSM to future E changes over the northern mid- to high latitudes.

5. Summary and remarks

In this study, we investigated the hydroclimatic and drought changes and their key drivers over global land by the late twenty-first century projected by 25 CMIP6 models under a moderate (SSP2-4.5) and a high (SSP5-8.5) emissions scenario. We first examined and compared the multimodel ensemble mean (MMM) change patterns in annual precipitation (P), evapotranspiration (E), surface (top 10 cm) and total soil moisture (SM), surface and total runoff (R), and self-calibrated Palmer drought severity index with Penman–Monteith PET (scPDSIpm), and then the changes in agricultural and hydrological drought characteristics (frequency, duration, and area) defined by scPDSIpm, SM, and R from the current (1970–99) to future (2070–99) periods. We then examined the contributions from the key drivers to the future hydroclimatic changes under the two emissions scenarios, which show similar change patterns with larger magnitudes under SSP5-8.5. The main findings are summarized as follows.

The MMM change patterns for annual P, E, surface and total SM and R, and scPDSMpm are broadly comparable to those of CMIP5 models (Collins et al. 2013; Zhao and Dai 2015), with increased P and E (by 5%–50%) over most Eurasia, North America, and Africa, except for the Mediterranean region, southern Africa, and northwest North America–Central America–northern South America, where P and E decrease. Decreased P is projected over most Australia where E changes are small. Widespread decreases in surface SM are seen over most of the Americas, Europe, Australia, southern Africa, Southeast and north Asia, likely due to ubiquitous PET increases and decreased P over many subtropical regions under global warming. Total SM shows less widespread drying than surface SM, with decreases mainly over southwest North America, Central America, most of South America, the Mediterranean region, southern Africa, and Australia. Surface and total SM increase over East and Central Africa, India, and the Arabian Peninsula. Total runoff changes are comparable to CMIP5 results (Zhao and Dai 2015), with large increases (by 20%–60%) over East and Central Africa, the Arabian Peninsula, India, central and eastern Asia, Alaska, and southeast South America, but decreases over the Mediterranean region, central North America, Central America, central and northern South America, and southern Africa. Changes in surface runoff are comparable with the total runoff changes, except for more widespread decreases over Europe and western Asia and central North America. The scPDSIpm mean changes generally follow those of surface SM, except for some wetting over northern high latitudes that are absent in surface SM. The scPDSIpm changes are also broadly comparable to those from CMIP5 models (Zhao and Dai 2015).

Besides the mean changes, there is also widespread flattening of the probability distribution functions (PDFs) of the scPDSIpm, surface and total SM and R by the late twenty-first century under both the SSP2-4.5 and SSP5-8.5 scenarios, similar

Brought to you by SUNY ALBANY LIBR SB23 | Unauthenticated | Downloaded 01/06/22 06:58 PM UTC

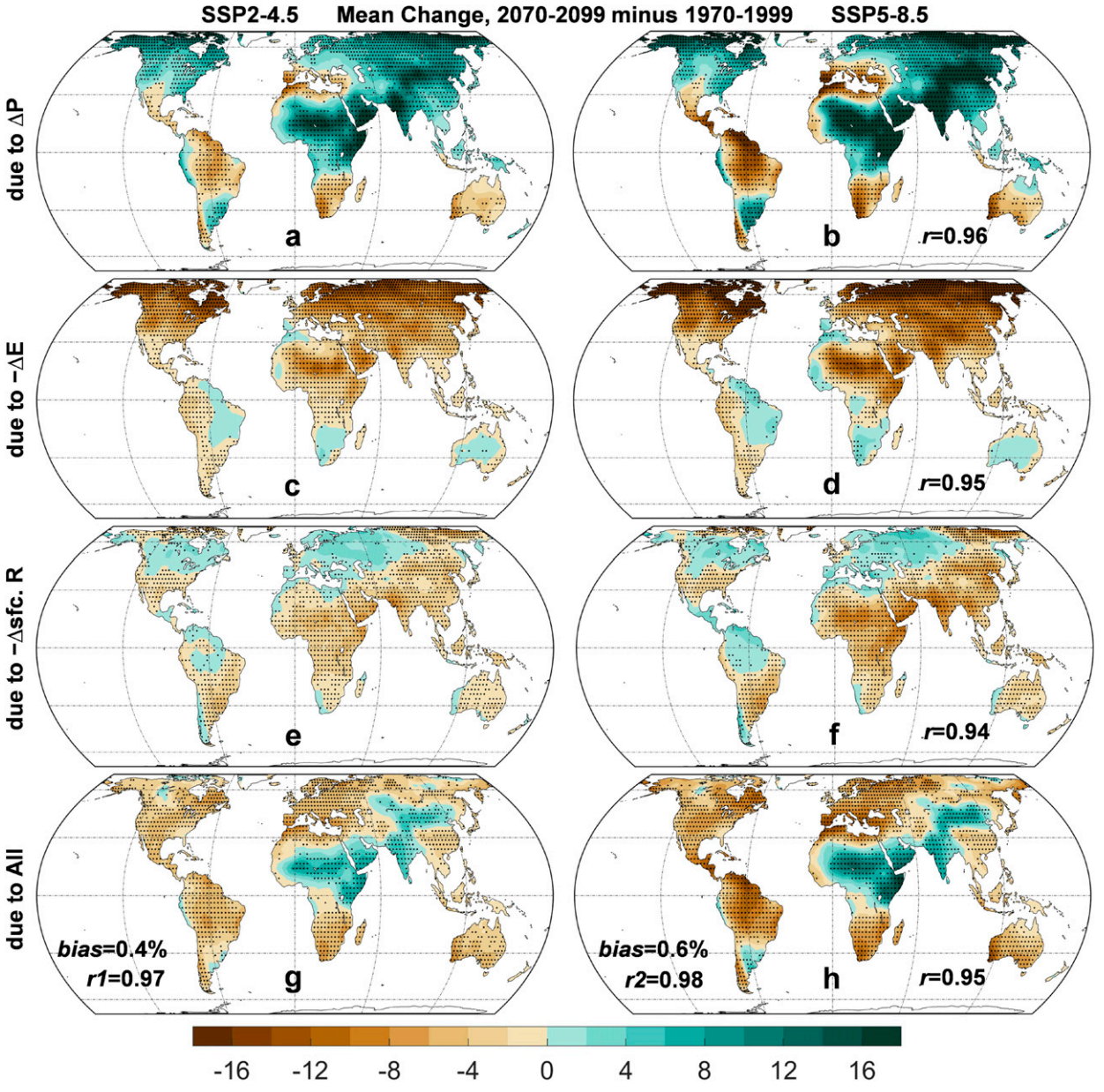

FIG. 11. Attribution of the top-10-cm-layer annual soil moisture (SM) changes (in % of the MMM for 1970–99) from 1970–99 to 2070–99 under the (left) SSP2-4.5 and (right) SSP5-8.5 scenario to changes in (a),(b) precipitation (ΔP); (c),(d) evapotranspiration (ΔE); (e),(f) surface runoff (ΔSR); and (g),(h) the sum of the ΔP, ΔE, and ΔSR contributions (All). The attribution was done for each model, and then averaged over the 21 models. The pattern correlation (r) between the two scenarios is also shown in the right panels. The pattern correlations (r1 and r2) between the total attributed and model-projected changes are shown in (g) and (h), and the global mean of the total attributed changes shown in (g) and (h) is more than that of the model-projected SM changes (shown in Figs. 2a,b) by 0.4% and 0.6%, respectively, under SSP2-4.5 and SSP5-8.5. The stippling indicates at least 80% of the models agreeing on the sign of change.

to those seen in CMIP5 models (Zhao and Dai 2015). The flattening is most pronounced over the northern high latitudes, northern Africa, and the Middle East for all the hydroclimatic fields. In particular, the SD increase and peak-frequency decrease based on both surface and total R are especially large. Such PDF flattening, combined with any mean decreases, would lead to large increases in drought events. To a large extent, the PDF flattening results from future changes in the mean annual cycle, although it is unclear whether and how it may be linked to the PDF flattening and the annual cycle change in surface air temperatures (Chen et al. 2019).

Agricultural drought frequencies defined using the current (1970–99) 20th percentile of the scPDSIpm and SM anomalies suggest widespread increases by ~25%–100% (50%–200%)

Brought to you by SUNY ALBANY LIBR SB23 | Unauthenticated | Downloaded 01/06/22 06:58 PM UTC

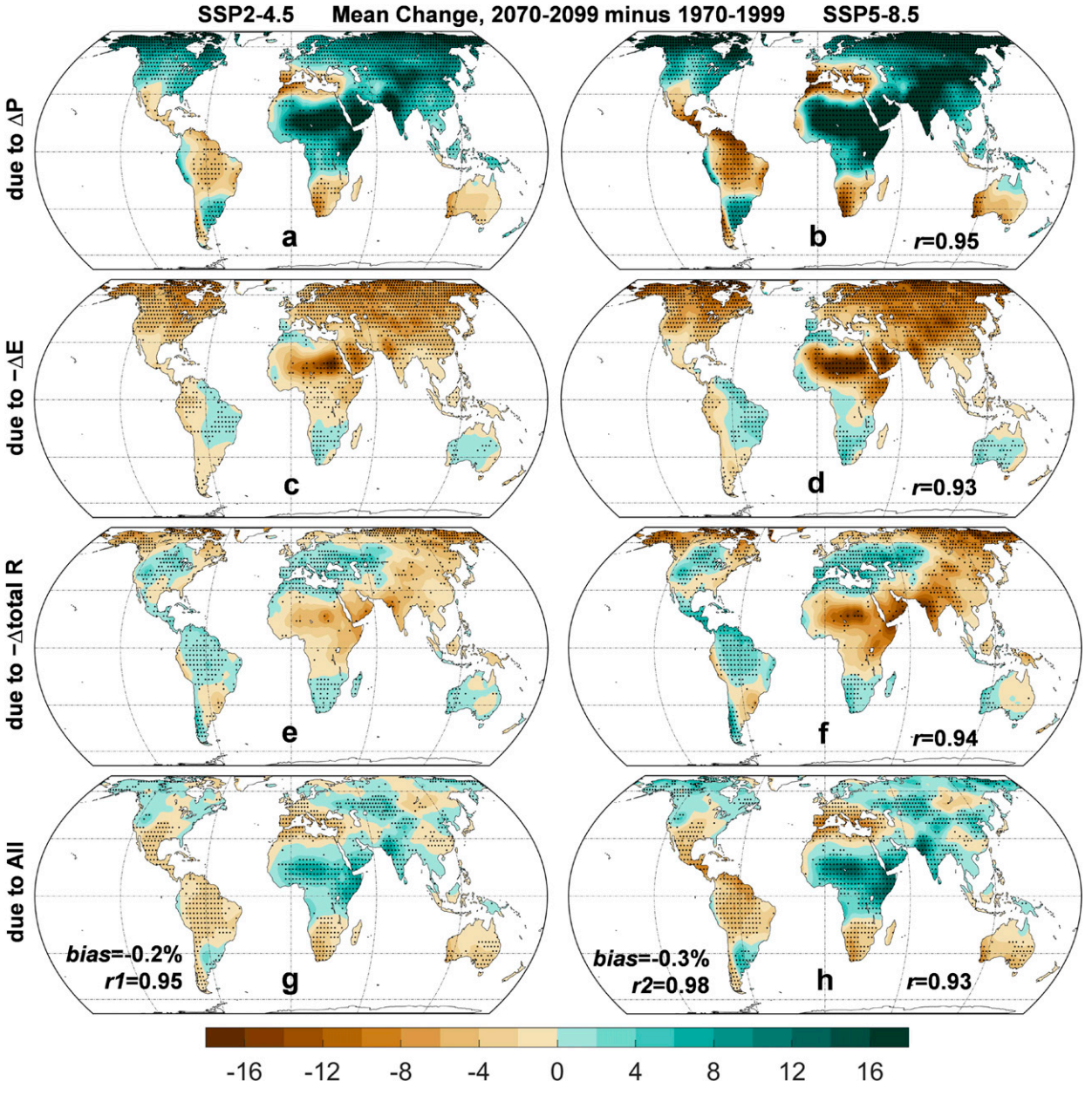

FIG. 12. As in Fig. 11, but for attribution of total soil moisture (SM) annual changes. The global mean of the total attributed changes is less than that of the model-projected SM changes (shown in Figs. 2c,d) by 0.2% and 0.3%, respectively, under SSP2-4.5 and SSP5-8.5.

under the SSP2-4.5 (SSP5-8.5) scenario by the late twenty-first century over most land areas (except East Africa, parts of North Africa, and India). The largest drought frequency increases are seen over the Amazon and northern South America, Europe and the Mediterranean region, southern Africa, North America, Central America, Southeast Asia, and Australia. Along with the increased frequency, the duration of the agricultural droughts based on scPDSIpm or surface SM would also increase by 0.2–3.0 (0.5–5.0) months by the late twenty-first century under the SSP2-4.5 (SSP5-8.5) scenario. These drought increases result from both a mean shift (toward drier conditions) over many subtropical areas and the widespread PDF flattening. Changes in the frequency and duration of the runoff-based hydrological drought are smaller and less widespread, but increases are still considerable and robust over most of the Americas, Europe, and southern Africa. The global percentage area under agricultural drought conditions based on scPDSIpm is projected to increase from 20% to about 28% (35%) under the SSP2-4.5 (SSP5-8.5) scenario from 1950–2100, compared with the increases to 30%–35% (33%–39%) based on normalized SM with surface

Brought to you by SUNY ALBANY LIBR SB23 | Unauthenticated | Downloaded 01/06/22 06:58 PM UTC

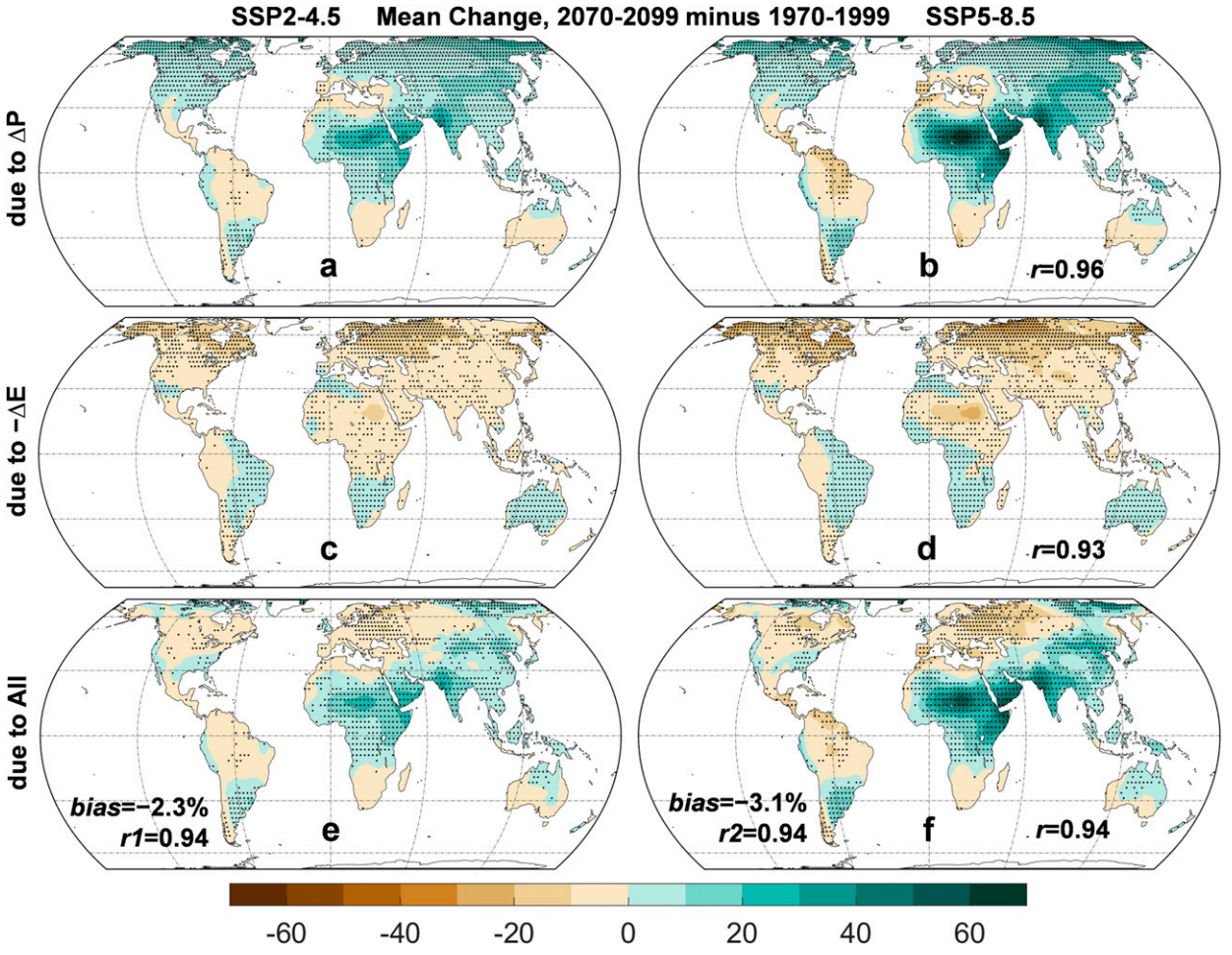

FIG. 13. As in Fig. 11, but for attribution of surface runoff (R) annual changes due to (a),(b) ΔP; (c),(d) ΔE; and (e),(f) their sum. The global mean of the total attributed changes with is less than that of the model-projected surface R changes (shown in Figs. 2e,f) by 2.3% and 3.1%, respectively, under SSP2-4.5 and SSP5-8.5.

SM indicating the largest increase. Global areas under hydrological drought would increase only slightly, from ~20% to ~25%–26% under the SSP5-8.5 scenario.

Our attribution analysis suggests that the scPDSIpm decrease (i.e., drying) results mainly from increased surface vapor pressure deficits (which increase PET) over the globe, with additional weak drying from increased solar radiation over most of the Americas, Europe, Africa, and Australia, while P increases over most Eurasia, North America, and Africa (except for the subtropical drying regions) lead to increased scPDSIpm (i.e., wetting). Changes in both surface and total SM are attributed mainly to P and E changes, while the surface and total R changes are determined primarily by the P changes with some drying effect from increased E mainly over northern mid- to high latitudes. Large E changes are attributed primarily to increases in atmospheric demand of moisture (i.e., PET), with some negative effect from decreases in surface soil moisture over the Americas, Europe, southern Africa, and Australia.

Despite the recent developments in climate models since CMIP5, our CMIP6 results are largely consistent with the CMIP5 model results reported previously (Zhao and Dai 2015; Berg et al. 2017; Zhao and Dai 2017; Dai et al. 2018). This suggests that the widespread drying and increases in agricultural droughts over most of the Americas (including the Amazon), Europe and the Mediterranean region, southern Africa, Southeast Asia, and Australia are robust response to the warming under moderate-to-high emissions scenarios. Similar to CMIP5 results, the increase in drought events (i.e., extremes) results from both the decrease in the mean (i.e., drying) and the flattening of the PDFs (i.e., increased variability, mainly due to increased annual cycle) of the aridity metrics. Our results also reaffirm the conclusions based on 13 CMIP6 models by Cook et al. (2020), who highlighted many of the same regions that are most likely to be at risk of increased drought in the twenty-first century and areas where hydroclimatic changes are either small or indicate wetter conditions (e.g., over East Africa and India). The more widespread drying suggested by surface SM than total SM is also in agreement with Berg et al. (2017) and Cook et al. (2020), likely due to the larger impact of the increased PET on surface SM and stronger controls by vegetation on subsurface

Brought to you by SUNY ALBANY LIBR SB23 | Unauthenticated | Downloaded 01/06/22 06:58 PM UTC

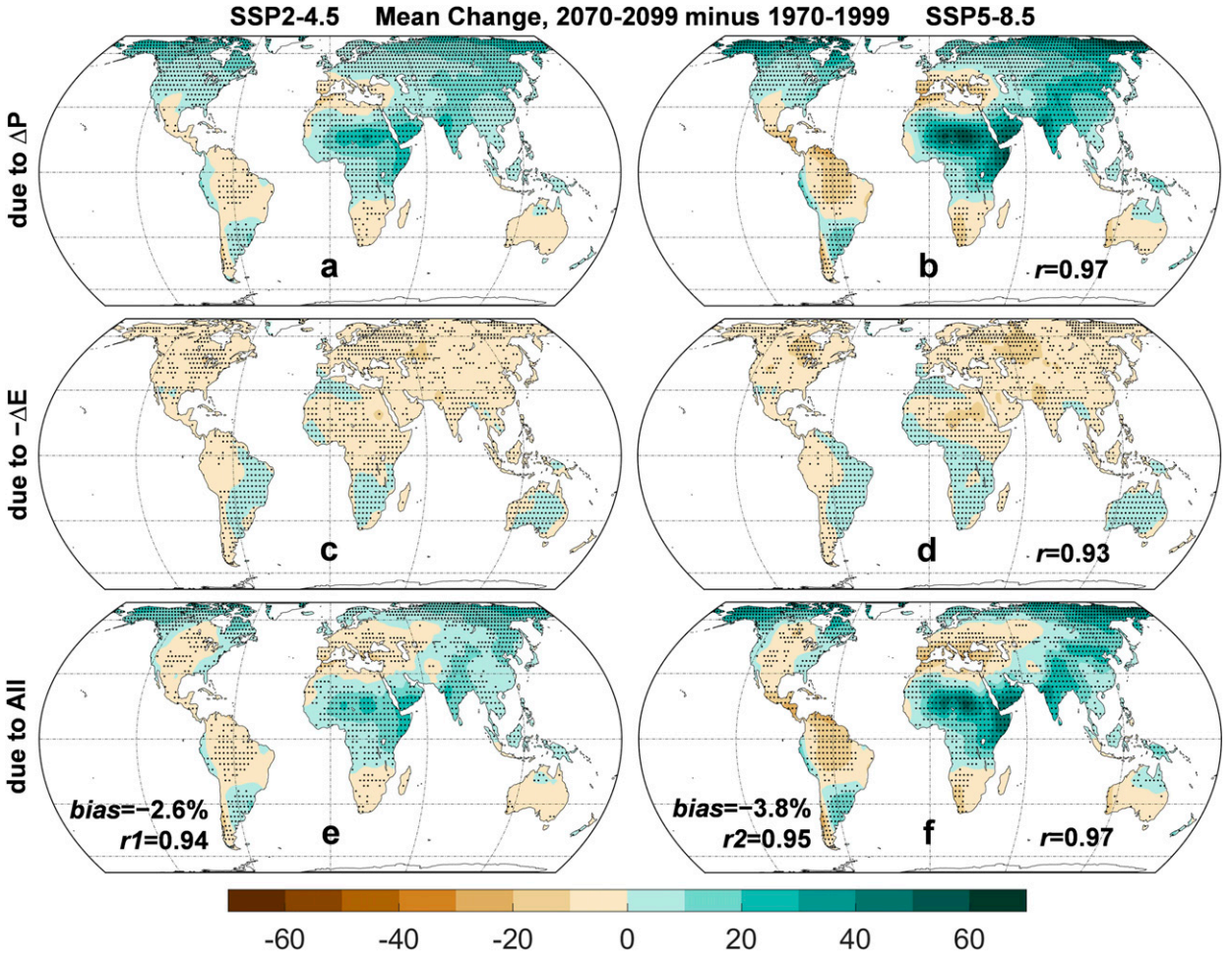

FIG. 14. As in Fig. 13, but for attribution of total runoff (R) annual changes. The global mean of the total attributed changes is less than that of the model-projected R changes (shown in Figs. 2g,h) by 2.6% and 3.8%, respectively, under SSP2-4.5 and SSP5-8.5.

soil moisture. We noticed, however, that the soil moisture and runoff changes vary greatly among individual CMIP6 model simulations, especially over central and northern Africa, likely partly due to realization-dependent internal variability associated with precipitation (Dai and Bloecker 2019). This also highlights the need for offline calculations of different aridity measures for quantifying future hydroclimatic changes (Prudhomme et al. 2014).

We also noticed that, while the broad drying patterns are very similar between CMIP6 and CMIP3 or CMIP5 models (e.g., Wang 2005; Burke et al. 2006; Burke and Brown 2008; Sheffield and Wood 2008; Dai 2011a, 2013a; Taylor et al. 2013; Prudhomme et al. 2014; Berg et al. 2017; Cook et al. 2014, 2018; Zhao and Dai 2015, 2017), the increases in soil moisture and runoff over East and central-northern Africa, India, and the Arabian Peninsula are larger and more widespread in CMIP6 than CMIP5 projections. The exact cause of this difference requires further investigation. Furthermore, precipitation and other hydroclimatic changes over northern Australia and other transition zones between the subtropical dry zone and the lower/higher latitudes can be highly model dependent and uncertain. However, the widespread flattening of the probability distribution functions and thus increased variability for all the hydroclimatic fields appear to be a robust response to GHG-induced global warming in both the CMIP5 and CMIP6 models, but its underlying cause needs further investigation.

Acknowledgments. The authors thank the three anonymous reviewers for their constructive comments that have helped improve the paper, the World Climate Research Programme's Working Group on Coupled Modelling, which is responsible for CMIP, and the climate modeling groups (listed in Table 1 of this paper) for producing and making available their model output. Zhao was supported by the National Basic Research Program of China (2018YFC1507704), the Strategic Priority Research Program of Chinese Academy of Sciences (XDA20020201), and the National Natural Science Foundation of China (41675094, 41975115). Dai was supported by the National Science Foundation (Grants AGS-2015780 and OISE-1743738) and the National Oceanic and Atmospheric Administration (Award NA18OAR4310425).

Brought to you by SUNY ALBANY LIBR SB23 | Unauthenticated | Downloaded 01/06/22 06:58 PM UTC

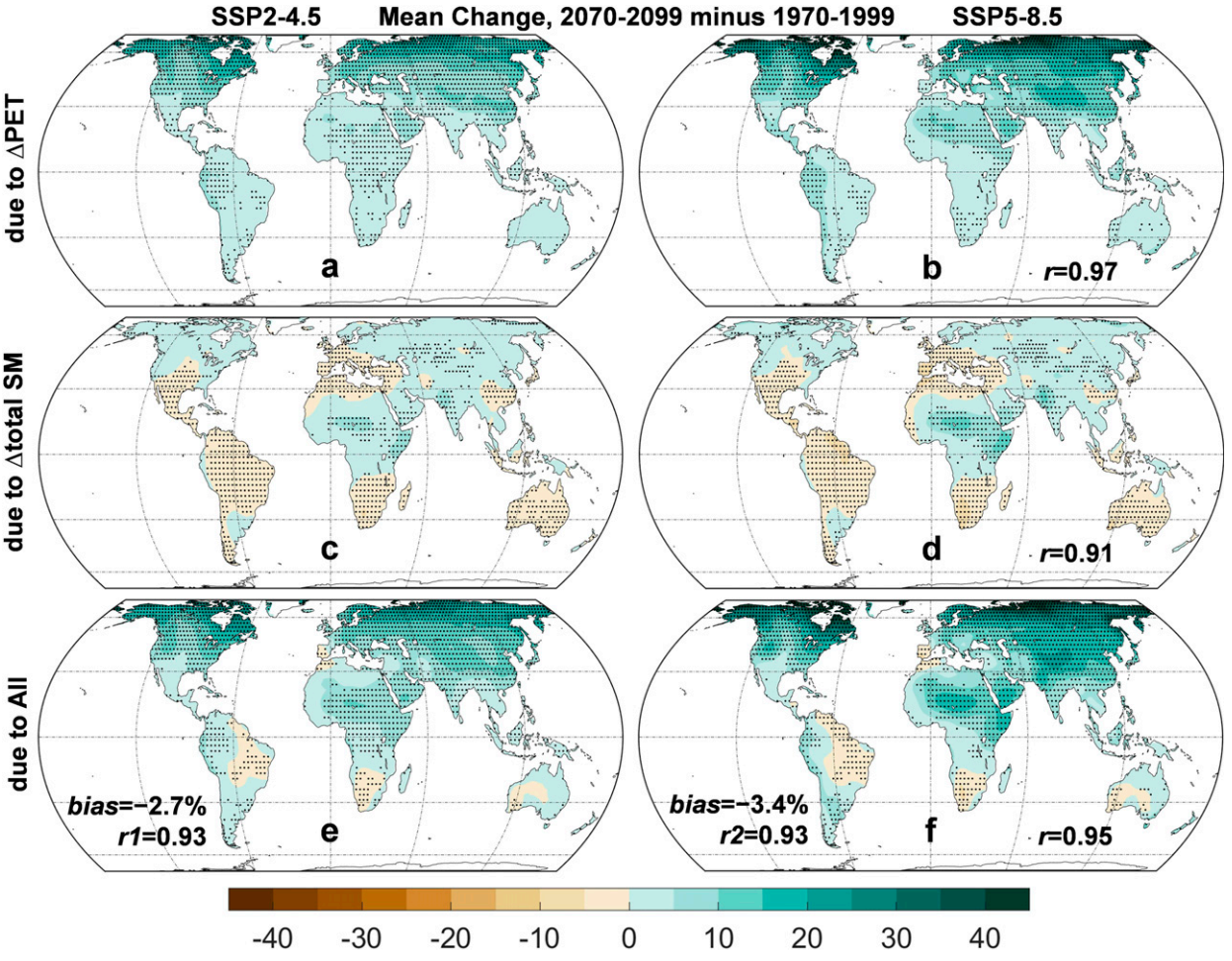

FIG. 15. As in Fig. 11, but for attribution of annual evapotranspiration (E) changes due to changes in (a),(b) PET and (c),(d) total soil moisture (SM). The global mean of the total attributed changes is less than that of the model-projected E changes (shown in Figs. 1c,d) by 2.7% and 3.4%, respectively, under SSP2-4.5 and SSP5-8.5.

Data availability statement. All the model data were downloaded from the CMIP6 data archive (https://esgf-node.llnl.gov/search/cmip6/). The scPDSIpm data were available from http://www.atmos.albany.edu/facstaff/adai/data/PDSI-CMIP6/.

REFERENCES

Berg, N., and A. Hall, 2017: Anthropogenic warming impacts on California snowpack during drought. *Geophys. Res. Lett.*, **44**, 2511–2518, https://doi.org/10.1002/2016GL072104.

Berg, A., J. Sheffield, and P. C. D. Milly, 2017: Divergent surface and total soil moisture projections under global warming. *Geophys. Res. Lett.*, **44**, 236–244, https://doi.org/10.1002/2016GL071921.

Burke, E. J., and S. J. Brown, 2008: Evaluating uncertainties in the projection of future drought. *J. Hydrometeor.*, **9**, 292–299, https://doi.org/10.1175/2007JHM929.1.

——, ——, and N. Christidis, 2006: Modeling the recent evolution of global drought and projections for the twenty-first century with the Hadley Centre climate model. *J. Hydrometeor.*, **7**, 1113–1125, https://doi.org/10.1175/JHM544.1.

Chen, J., A. Dai, and Y. Zhang, 2019: Projected changes in daily variability and seasonal cycle of near-surface air temperature over the globe during the twenty-first century. *J. Climate*, **32**, 8537–8561, https://doi.org/10.1175/JCLI-D-19-0438.1.

——, ——, ——, and K. L. Rasmussen, 2020: Changes in the convective potential available energy and convective inhibition under global warming. *J. Climate*, **33**, 2025–2050, https://doi.org/10.1175/JCLI-D-19-0461.1.

Chou, C., J. D. Neelin, C.-A. Chen, and J.-Y. Tu, 2009: Evaluating the "rich-get-richer" mechanism in tropical precipitation change under global warming. *J. Climate*, **22**, 1982–2005, https://doi.org/10.1175/2008JCLI2471.1.

Collins, M., and Coauthors, 2013: Long-term climate change: Projections, commitments and irreversibility. *Climate Change 2013: The Physical Science Basis*, T. F. Stocker et al., Eds., Cambridge University Press, 1029–1136.

Cook, B. I., J. E. Smerdon, R. Seager, and S. Coats, 2014: Global warming and 21st century drying. *Climate Dyn.*, **43**, 2607–2627, https://doi.org/10.1007/s00382-014-2075-y.

——, T. R. Ault, and J. E. Smerdon, 2015: Unprecedented 21st century drought risk in the American Southwest and Central Plains. *Sci. Adv.*, **1**, e1400082, https://doi.org/10.1126/sciadv.1400082.

Brought to you by SUNY ALBANY LIBR SB23 | Unauthenticated | Downloaded 01/06/22 06:58 PM UTC

——, J. S. Mankin, and K. J. Anchukaitis, 2018: Climate change and drought: From past to future. *Curr. Climate Change Rep.*, **4**, 164–179, https://doi.org/10.1007/s40641-018-0093-2.

——, ——, K. Marvel, A. P.Williams, J. E. Smerdon, and K. J. Anchukaitis, 2020: Twenty-first century drought projections in the CMIP6 forcing scenarios. *Earth's Future*, **8**, e2019EF001461, https://doi.org/10.1029/2019EF001461.

Dai, A., 2011a: Drought under global warming: A review. *Wiley Interdiscip. Rev.: Climate Change*, **2**, 45–65, https://doi.org/10.1002/wcc.81.

——, 2011b: Characteristics and trends in various forms of the Palmer drought severity index during 1900–2008. *J. Geophys. Res.*, **116**, D12115, https://doi.org/10.1029/2010JD015541.

——, 2013a: Increasing drought under global warming in observations and models. *Nat. Climate Change*, **3**, 52–58, https://doi.org/10.1038/nclimate1633.

——, 2013b: The influence of the inter-decadal Pacific Oscillation on U.S. precipitation during 1923–2010. *Climate Dyn.*, **41**, 633–646, https://doi.org/10.1007/s00382-012-1446-5.

——, 2021: Hydroclimatic trends during 1950–2018 over global land. *Climate Dyn.*, **56**, 4027–4049, https://doi.org/10.1007/s00382-021-05684-1.

——, and T. Zhao, 2017: Uncertainties in historical changes and future projections of drought. Part I: Estimates of historical drought changes. *Climatic Change*, **144**, 519–533, https://doi.org/10.1007/s10584-016-1705-2.

——, and C. E. Bloecker, 2019: Impacts of internal variability on temperature and precipitation trends in large ensemble simulations by two climate models. *Climate Dyn.*, **52**, 289–306, https://doi.org/10.1007/s00382-018-4132-4.

——, and J. Deng, 2021: Arctic amplification weakens the variability of daily temperatures over northern mid-to-high latitudes. *J. Climate*, **34**, 2591–2609, https://doi.org/10.1175/JCLI-D-20-0514.1.

——, T. Zhao, and J. Chen, 2018: Climate change and drought: A precipitation and evaporation perspective. *Curr. Climate Change Rep.*, **4**, 301–312, https://doi.org/10.1007/s40641-018-0101-6.

Donat, M. G., and L. V. Alexander, 2012: The shifting probability distribution of global daytime and night-time temperatures. *Geophys. Res. Lett.*, **39**, L14707, https://doi.org/10.1029/2012GL052459.

Easterling, D. R., G. A. Meehl, C. Parmesan, S. A. Changnon, and L. O. Mearns, 2000: Climate extremes: Observations, modeling and impacts. *Science*, **289**, 2068–2074, https://doi.org/10.1126/science.289.5487.2068.

Eyring, V., S. Bony, G. A. Meehl, C. A. Senior, B. Stevens, R. J. Stouffer, and K. E. Taylor, 2016: Overview of the Coupled Model Intercomparison Project Phase 6 (CMIP6) experimental design and organization. *Geosci. Model Dev.*, **9**, 1937–1958, https://doi.org/10.5194/gmd-9-1937-2016.

Feng, S., and Q. Fu, 2013: Expansion of global drylands under warming climate. *Atmos. Chem. Phys.*, **13**, 10 081–10 094, https://doi.org/10.5194/acp-13-10081-2013.

Fu, Q., and S. Feng, 2014: Responses of terrestrial aridity to global warming. *J. Geophys. Res. Atmos.*, **119**, 7863–7875, https://doi.org/10.1002/2014JD021608.

Giorgi, F., E. Coppola, and F. Raffaele, 2018: Threatening levels of cumulative stress due to hydroclimatic extremes in the 21st century. *Climate Atmos. Sci.*, **1**, 18, https://doi.org/10.1038/s41612-018-0028-6.

Hoerling, M., J. Eischeid, J. Perlwitz, X. Quan, T. Zhang, and P. Pegion, 2012: On the increased frequency of mediterranean drought. *J. Climate*, **25**, 2146–2161, https://doi.org/10.1175/JCLI-D-11-00296.1.

Knutti, R., and J. Sedlacek, 2013: Robustness and uncertainties in the new CMIP5 climate model projections. *Nat. Climate Change*, **3**, 369–373, https://doi.org/10.1038/nclimate1716.

Lee, J.-Y., and B. Wang, 2014: Future change of global monsoon in the CMIP5. *Climate Dyn.*, **42**, 101–119, https://doi.org/10.1007/s00382-012-1564-0.

Lu, J., G. A. Vecchi, and T. J. Reichler, 2007: Expansion of the Hadley cell under global warming. *Geophys. Res. Lett.*, **34**, L06805, https://doi.org/10.1029/2006GL028443.

Meinshausen, M., and Coauthors, 2020: The shared socio-economic pathway (SSP) greenhouse gas concentrations and their extensions to 2500. *Geosci. Model Dev.*, **13**, 3571–3605, https://doi.org/10.5194/gmd-13-3571-2020.

Palmer, W. C., 1965: Meteorological drought. U.S. Weather Bureau Research Paper 45, 58 pp., http://www.ncdc.noaa.gov/temp-and-precip/drought/docs/palmer.pdf.

Prudhomme, C., and Coauthors, 2014: Hydrological droughts in the 21st century, hotspots and uncertainties from a global multimodel ensemble experiment. *Proc. Natl. Acad. Sci. USA*, **111**, 3262–3267, https://doi.org/10.1073/pnas.1222473110.

Scheff, J., and D. M. W. Frierson, 2012: Robust future precipitation declines in CMIP5 largely reflect the poleward expansion of model subtropical dry zones. *Geophys. Res. Lett.*, **39**, L18704, https://doi.org/10.1029/2012GL052910.

——, and ——, 2014: Scaling potential evapotranspiration with greenhouse warming. *J. Climate*, **27**, 1539–1558, https://doi.org/10.1175/JCLI-D-13-00233.1.

——, and ——, 2015: Terrestrial aridity and its response to greenhouse warming across CMIP5 climate models. *J. Climate*, **28**, 5583–5600, https://doi.org/10.1175/JCLI-D-14-00480.1.

——, J. S. Mankin, S. Coats, and H. Liu, 2021: CO_2-plant effects do not account for the gap between dryness indices and projected dryness impacts in CMIP6 or CMIP5. *Environ. Res. Lett.*, **16**, 034018, https://doi.org/10.1088/1748-9326/abd8fd.

Seager, R., T. J. Osborn, Y. Kushnir, I. R. Simpson, J. Nakamura, and H. Liu, 2019: Climate variability and change of Mediterranean-type climates. *J. Climate*, **32**, 2887–2915, https://doi.org/10.1175/JCLI-D-18-0472.1.

Seth, A., S. A. Rauscher, M. Biasutti, A. Giannini, S. J. Camargo, and M. Rojas, 2013: CMIP5 projected changes in the annual cycle of precipitation in monsoon regions. *J. Climate*, **26**, 7328–7351, https://doi.org/10.1175/JCLI-D-12-00726.1.

Sheffield, J., and E. F. Wood, 2008: Projected changes in drought occurrence under future global warming from multi-model, multi-scenario, IPCC AR4 simulations. *Climate Dyn.*, **31**, 79–105, https://doi.org/10.1007/s00382-007-0340-z.

Shuttleworth, W. J., 1993: Evaporation. *Handbook of Hydrology*, D. R. Maidment, Ed., McGraw-Hill, 4.1–4.53.

Swann, A. L. S., F. M. Hoffman, C. D. Koven, and J. T. Randerson, 2016: Plant responses to increasing CO_2 reduce estimates of climate impacts on drought severity. *Proc. Natl. Acad. Sci. USA*, **113**, 10 019–10 024, https://doi.org/10.1073/pnas.1604581113.

Taylor, I. H., E. Burke, L. McColl, P. D. Falloon, G. R. Harris, and D. McNeall, 2013: The impact of climate mitigation on projections of future drought. *Hydrol. Earth Syst. Sci.*, **17**, 2339–2358, https://doi.org/10.5194/hess-17-2339-2013.

Ting, M., R. Seager, C. Li, H. Liu, and N. Henderson, 2018: Mechanism of future spring drying in the southwestern United States in CMIP5 models. *J. Climate*, **31**, 4265–4279, https://doi.org/10.1175/JCLI-D-17-0574.1.

Brought to you by SUNY ALBANY LIBR SB23 | Unauthenticated | Downloaded 01/06/22 06:58 PM UTC

Trenberth, K. E., L. Smith, T. Qian, A. Dai, and J. Fasullo, 2007: Estimates of the global water budget and its annual cycle using observational and model data. *J. Hydrometeor.*, **8**, 758–769, https://doi.org/10.1175/JHM600.1.

van Vuuren, D. P., and Coauthors, 2011: The representative concentration pathways: An overview. *Climatic Change*, **109**, 5–31, https://doi.org/10.1007/s10584-011-0148-z.

Vicente-Serrano, S. M., T. R. Mc, D. G. Vicar, Y. Miralles, Y. Yang, and M. Tomas-Burguera, 2020: Unraveling the influence of atmospheric evaporative demand on drought and its response to climate change. *Wiley Interdiscip. Rev.: Climate Change*, **11**, e632, https://doi.org/10.1002/wcc.632.

Wang, G. L., 2005: Agricultural drought in a future climate: Results from 15 global climate models participating in the IPCC 4th assessment. *Climate Dyn.*, **25**, 739–753, https://doi.org/10.1007/s00382-005-0057-9.

Wehner, M., D. R. Easterling, J. H. Lawrimore, R. R. Heim, R. S. Vose, and B. D. Santer, 2011: Projections of future drought in the continental United States and Mexico. *J. Hydrometeor.*, **12**, 1359–1377, https://doi.org/10.1175/2011JHM1351.1.

Wells, N., S. Goddard, and M. J. Hayes, 2004: A self-calibrating Palmer drought severity index. *J. Climate*, **17**, 2335–2351, https://doi.org/10.1175/1520-0442(2004)017<2335:ASPDSI>2.0.CO;2.

Zhang, W., T. Zhou, L. Zhang, and L. Zou, 2019: Future intensification of the water cycle with an enhanced annual cycle over global land monsoon regions. *J. Climate*, **32**, 5437–5452, https://doi.org/10.1175/JCLI-D-18-0628.1.

Zhao, T., and A. Dai, 2015: The magnitude and causes of global drought changes in the 21st century under a low–moderate emissions scenario. *J. Climate*, **28**, 4490–4512, https://doi.org/10.1175/JCLI-D-14-00363.1.

——, and ——, 2017: Uncertainties in historical changes and future projections of drought. Part II: Model simulated historical and future drought changes. *Climatic Change*, **144**, 535–548, https://doi.org/10.1007/s10584-016-1742-x.

Brought to you by SUNY ALBANY LIBR SB23 | Unauthenticated | Downloaded 01/06/22 06:58 PM UTC